Seamless simulation of multiphase flow, poromechanics, and seismic deformation in fractured subsurface formations

Zheng Han[1], Guotong ren[1], and Rami M Younis[1]

[1]The University of Tulsa

November 23, 2022

Abstract

A seamless numerical model of coupled multiphase flow and inertial mechanics in fractured porous media is proposed. The model develops an automatic time step size control method to efficiently and accurately capture transitions between flow with small deformation, quasi-static slip, and dynamic rupture with seismic wave propagation. The model utilizes a mixed and embedded approach that represents fractures explicitly. The mixed discretization combines an extended finite element method (XFEM) with a projection embedded discrete fracture and matrix (pEDFM) finite volume method. Mechanical inertia is approximated implicitly using a stable Newmark scheme, and fracture contact constraints for stick-slip conditions are enforced by a Lagrange Multiplier approach that is stabilized by Polynomial Pressure Projection (PPP). The temporal adaption method combines discretization error, Coulomb friction, and slip rate considerations to capture pre-seismic triggering, co-seismic spontaneous rupture, and arrest. The model is applied to simulate multiple cycles of induced seismic rupture under various multiphase fluid production and injection scenarios. This is enabled by time step size control to automatically span transitions across seven orders of magnitude in timescales.

Seamless simulation of multiphase flow, poromechanics, and seismic deformation in fractured subsurface formations

Zheng Han[1], Guotong Ren[1], and Rami M. Younis[1]

[1]800 S Tucker Dr, Tulsa, OK 74104

Key Points:

- A seamless numerical model is developed to approximate coupled multiphase flow and transient poromechanics in fractured reservoirs using an embedded mesh approach.
- A temporal control method is developed to simultaneously consider accuracy, slippage, and slip rate, and it is applied to accurately capture pre-seismic triggering, co-seismic spontaneous rupture, and rupture arrest, as well as multiple cycles of these. This is accomplished by the method's ability to accurately recognize transitions and to rapidly adapt time scales across seven orders of magnitude.
- The robustness, efficiency, and sensitivity to prescribed parameters are investigated empirically in capturing reactivation and nucleation seismic rupture under fluid injection.

Corresponding author: Rami M. Younis, `rami-younis@utulsa.edu`

Abstract

A seamless numerical model of coupled multiphase flow and inertial mechanics in fractured porous media is proposed. The model develops an automatic time step size control method to efficiently and accurately capture transitions between flow with small deformation, quasi-static slip, and dynamic rupture with seismic wave propagation. The model utilizes a mixed and embedded approach that represents fractures explicitly. The mixed discretization combines an extended finite element method (XFEM) with a projection embedded discrete fracture and matrix (pEDFM) finite volume method. Mechanical inertia is approximated implicitly using a stable Newmark scheme, and fracture contact constraints for stick-slip conditions are enforced by a Lagrange Multiplier approach that is stabilized by Polynomial Pressure Projection (PPP). The temporal adaption method combines discretization error, Coulomb friction, and slip rate considerations to capture pre-seismic triggering, co-seismic spontaneous rupture, and arrest. The model is applied to simulate multiple cycles of induced seismic rupture under various multiphase fluid production and injection scenarios. This is enabled by time step size control to automatically span transitions across seven orders of magnitude in timescales.

1 Introduction

Subsurface engineering systems are the subject of fluid injection or production and mechanical forcing at various stages of their operation. These activities drive complex multiphase flow and deformation dynamics across multiple scales and extents. Depending on the particular engineering or scientific objectives, the modeler will select a suitable system model by ignoring specific effects deemed negligible within the intended range of operating parameters under study. This practice is not only beneficial for parametric simplification but also toward realizing timely computational workflows. An example of this practice is to use a coupled model for fluid flow and quasi-static mechanics when engineering resource recovery or subsurface storage operations and a distinct transient elastic deformation model to study seismic wave propagation occurring over a short duration. This work pertains to developing a seamless model spanning coupled multiphase fluid-flow and quasi-static deformation and seismic propagation and slip in the presence of fractures. The critical technical development is a temporal adaptivity algorithm to adapt the computational cost of simulation locally according to the underlying physical processes occurring throughout the simulation. Moreover, the adaptive algorithms enforce accurate and efficient simulation of either extreme (aseismic and seismic deformation), as well as any number of transitions to occur across them.
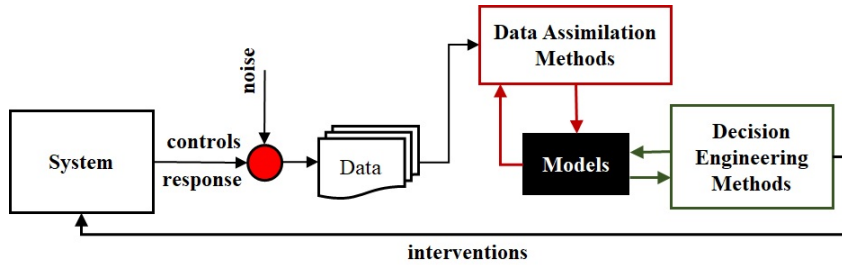

Figure 1: The closed-loop engineering cycle; after (Jansen et al., 2005, 2008). A target engineering system is observed and a model is reconciled with observations (red subcycle). The model is used to design and optimize engineering interventions that are subsequently applied to the system (green cycle).

A primary utility of this approach is in cases where: i) the operating parameter range is itself not known or limited *a priori*, and ii) when there is no adequate characterization of the conditions for which a particular set of physics (e.g., inertial mechanics) have marginal *versus* first-order effects. A prototypical example of an engineering application in which this is the case is the computer-assisted closed-loop reservoir management (CLRM) workflow illustrated in Figure 1. In the CLRM workflow, a model is continually reconciled with observations of the target system as they are acquired and through an iterative process (data assimilation). Subsequently, the reconciled models are used in another iterative process to design and optimize future engineering activity (decision engineering). The modeling component is subject to various plausible parameters or engineering control circumstances in these iterative sub-processes. Thus, the onus is to adapt continually and reconcile what physics to approximate or neglect while simultaneously expediting turn-around times.
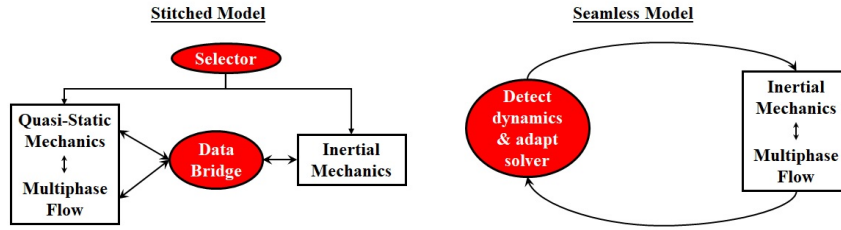
Figure 2: Illustration of two modeling approaches: a) stitched models apply either a flow simulation or seismic propagation model, and they provide approximate mechanisms to transfer state and parameter information between them; and b) seamless models encode a single set of equations and assumptions, and rely on internally adaptive solution methods to expedite computation.

As illustrated in Figure 2, two broad classes of simulation models may be applied. The first class, which we refer to as *stitched*, relies on coordination across two separate sub-models: one for coupled flow and quasi-static deformation and the other for seismic wave propagation. Selection logic is necessary to determine which limiting assumptions of either model are more appropriate for the scenario at hand. In the context of CLRM, further logic is necessary to enable the transfer of state and parameter information back-and-forth across the two models. In the contexts of both the data-assimilation and design workflows, observations can subsequently only inform a sub-model at a time. The proposed modeling approach is of the second class, which we refer to as *seamless*. The model applies a single set of governing models and constitutive relationships regardless of the simulation case at hand. Instead, the model relies on logic to adaptively determine suitable numerical solution approaches (especially time-step size). The goals of the automatic adaptations are to expedite computational performance while accurately honoring the local dynamics at hand. Time adaptivity is essential in this approach to efficiently and accurately capture the seismic process, given the vast disparity in characteristic scales between seismic deformation (e.g., milliseconds) and transient flow (e.g., hours). For example, if solution states and controls indicate minor deformation, the model would allow for large time-step sizes on the order of a month. Furthermore, as slow fault activation occurs, time-steps need to be adapted to capture quasi-static slip with sufficient accuracy to determine more precisely whether and when a transition to dynamic rupture will occur. Under inertial dynamic wave propagation, the model sufficiently refines time-steps to capture waveform information at receivers. Finally, the adaptivity allows for multiple cycles across changing operational controls.

Seamless modeling of quasi-static and dynamic hydromechanical processes at the system scale is challenging and understudied. Stitched models, on the other hand, have received considerable focus. These models combine independent advances in quasi-static hydromechanical simulation using the Biot theory of poroelasticity (Biot, 1941), with elastodynamic simulation.

Examples of quasi-static hydromechanical models and their application to periods before fault rupture include Jha and Juanes (2014); Cappa and Rutqvist (2011). Jha and Juanes (2014) developed a fixed-stress scheme to couple the hydrodynamic General Purpose Research Simulator (Cao, 2002) with the Pylith (Aagaard et al., 2013) mechanics model. The model was applied to investigate relationships between the pore pressure, fault-slip, and the onset of dynamic slip. Cappa and Rutqvist (2011) introduced a hydromechanical fault-permeability model into the coupled fluid flow and geomechanics simulator TOUGH–FLAC. The model itself links the finite-volume multiphase flow TOUGH2 model with the finite-difference geomechanics model FLAC3D. Despite excluding inertial effects, quasi-dynamic models augment quasi-static models with a shear-traction radiation damping term correlated with slip velocity. Quasi-dynamic models were applied to study unbounded and co-seismic fault-slip (Rice, 1993; Rice & Ben-Zion, 1996; Cueto-Felgueroso et al., 2017, 2018). However, given that inertial and viscous effects of fluids on wave propagation are ignored, Thomas et al. (2014) and Cueto-Felgueroso et al. (2018) show that quasi-dynamic models produce markedly different nucleation and rupture estimates compared to those obtained using fully dynamic approaches.

There are several reports of switching between a quasi-static model for the interseismic period to a dynamic rupture model for the co-seismic period. Cappa and Rutqvist (2012) for instance, switch from a quasi-static model once the shear stress state exceeds the static friction and transfer the simulated stress state at that point to initialize a dynamic rupture model. Similar switching strategies are also adopted by Buijze et al. (2017, 2019); Meng (2017); Meng and Wang (2018); Jin and Zoback (2018); Paap et al. (2020); Schwartzkopff et al. (2021) with variations in the quasi-static and dynamic models used. Buijze et al. (2017) model fluid injection indirectly by enforcing various pressure scenarios, and Buijze et al. (2019) show an application of the algorithm for natural gas production systems with faults. Meng (2017); Meng and Wang (2018) adopt an incompressible fluid model (steady flow) such that fluid properties and porosity do not change with pressure. Jin and Zoback (2018) modeled single-phase compressible fluid flow with a quasi-static coupled hydromechanical model. Paap et al. (2020) implement a coupled modeling approach using FLAC3D and SPECFEM2D and Schwartzkopff et al. (2021) develop a multiphase coupled quasi-static model and a dynamic mechanical model using the extended finite element method (XFEM). The switching criterion used is the length of the quasi-statically slipping patch along the fault.

Pampillón et al. (2018) report a seamless dynamic single-phase poroelastic model with an incompressible fluid. The model limited the time-step size adaptively according to slip rate, and its efficacy compared to a quasi-dynamic approach was demonstrated. This work develops a temporal adaptivity indicator to simultaneously consider contact traction, local discretization error, and slip rate to capture the fluid flow activity without fault-slip, pre-seismic triggering, co-seismic spontaneous rupture, and post-seismic arrest. Moreover, the method applies general multiphase and compressible flow in the matrix and fractures, fully dynamic poromechanics, fracture contact, and stick-slip conditions. The seamless model is validated, and we characterize the efficacy of the temporal adaptivity indicator for accuracy and computational efficiency. Finally, we apply the model to injection-induced aseismic and seismic slip scenarios and simultaneous injection and production scenarios in the presence of faults.

The proposed model extends an established quasi-static approach (Ren and Younis (2018); Ren et al. (2018)) that couples an extended finite element method (XFEM) (Khoei & Nikbakht, 2007; Khoei, 2014) approximation for mechanics with an Embedded Discrete Fracture and Matrix (EDFM) (Lee et al., 2001; Li & Lee, 2008; Moinfar et al., 2013) approximation for multi-phase fluid flow within the matrix and fractures. The particular projection-based variant (pEDFM) (Jiang & Younis, 2016b, 2017) is used to capture high contrast fracture-matrix cross-flows accurately. While the model was previously extended to accommodate fluid-driven fracture propagation (Ren & Younis, 2019, 2021a), this work neglects these effects. The model is extended to incorporate inertial terms, and a stable and second-order fully-implicit Newmark temporal discretization approximation is applied. Additionally, we develop a fracture contact model with fracture stick-slip behavior, and slip-weakening friction laws are adopted. The proposed methods treat contact forces in fractures using Lagrange Multiplier constraints, while a Polynomial Pressure Projection Method is adopted to stabilize the computation of contact traction. Finally, this work develops a temporal adaptivity indicator and time-step controller to simultaneously account for contact traction, local discretization error, and slip rate. We demonstrate that the method accurately captures fluid flow activity with fault-slip, pre-seismic triggering, co-seismic spontaneous rupture, as well as post-seismic arrest.

The article is organized as follows: in Section 2, the mathematical and numerical models are presented. In Section 3, we develop a hybrid time step selection scheme to simultaneously control discretization error, and capture sharp transitions across sticking, quasi-static slip, and dynamic rupture. In Section 4, we present several numerical studies to demonstrate that the proposed methods accurately capture transitions if and when they are to occur. Moreover, the temporal adaptivity ensures that the computational cost of the seamless model is comparable to the use of stitched models. Finally, Section 5 discusses implications of this work and summarizes the conclusions.

2 Governing Equations and Closure Relations

The proposed model considers a two-dimensional spatial domain containing several fractures. The outer boundary is closed to fluid flow, but mechanically, it admits free movement mimicking infinite extent under an initial, steady *in-situ* stress field (absorbing boundaries). Fractures are modeled as one-dimensional, non-intersecting, and piece-wise linear curves with an implied variable aperture along the length. Subsequently, the matrix domain treats fractures as embedded internal boundaries. We consider general multiphase flow within the matrix according to the quasi-static Darcy law with spatially variable permeability. The reference (initial) porosity field is spatially variable. A Lagrange variation model is applied whereby dynamic changes to porosity are related to the underlying rock deformation and pore pressure fields. The model captures inertial, linear poroelastic mechanics under the small deformation limit, and the Biot theory that relates the pore pressure field to the effective stress is applied. Mechanically, the aperture at a point on a fracture may be zero (contact) or positive (open). Moreover, a point along a fracture under a contact condition may either be sticking (insufficient traction to overcome friction) or slipping. In all computational examples presented, a slip-weakening friction model is applied. Fluid flow in open fracture locales is assumed to follow a nonlinear Poiseuille (lubrication limit) model. Fluid transfer between an open fracture and the surrounding matrix obeys a Darcy-type law and the transfer rate scales linearly with the local difference in pore pressure and fracture fluid pressure. Under fracture contact conditions, fluid flow in the matrix across fractures can be assumed to be zero (barriers to fluid flow) or follow the native matrix conductivity (non-sealing or open).

2.1 Preliminaries and mathematical notation

As illustrated in Figure 3a, we consider a two-dimensional open and bounded spatial domain, $\Omega \subset \mathbb{R}^2$, with outer-boundary $\partial\Omega$ and outward-oriented unit-normal field $\boldsymbol{n_m}(\partial\Omega)$. A collection of N_f fractures are represented by piece-wise linear segments that do not mutually intersect within their interiors. The fractures Γ_f are embedded within the matrix rock; i.e., the open matrix domain is defined as,

$$\Omega_m = \Omega - \bigcup_{f=1}^{N_f} \Gamma_f.$$

As illustrated in Figure 3b, fractures are oriented by local tangential coordinate
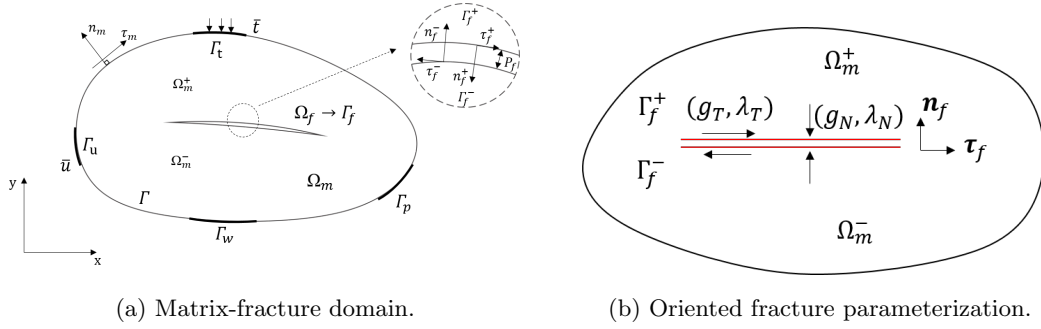

(a) Matrix-fracture domain.   (b) Oriented fracture parameterization.

Figure 3: Illustration of embedded fractures and notation.

frames. Let $l \geq 0$ denote the arc-length parameterization along a particular fracture Γ_f, as measured from a selected tip $\boldsymbol{x}_f^0$. Then the local unit-normal field $\boldsymbol{n_f}(\boldsymbol{x})$ is oriented with respect to the local tangent, $\boldsymbol{\tau_f}(l)$, and,

$$\boldsymbol{x}_f(l) = \boldsymbol{x}_f^0 + \int_0^l \boldsymbol{\tau_f}(\nu)\,d\nu \in \Gamma_f \ 1 \leq f \leq N_f.$$

The independent-state fields within the matrix are the fluid pore-pressure $P(\boldsymbol{x}, t)$, fluid phase-saturation $S_\eta(\boldsymbol{x}, t)$, and displacement $\boldsymbol{u}(\boldsymbol{x}, t)$ fields for $\boldsymbol{x} \in \Omega_m$ and $t \geq 0$. Note that while there are no restrictions to considering general multiphase flow, all computational examples assume the presence of a maximum of two immiscible fluid phases (i.e., $\eta \in \{0, 1\}$), and we neglect capillary effects. Within fractures, the independent state-fields are the fluid pressure $P_f(\boldsymbol{x}_f, t)$, and a phase volumetric fraction $S_{f,\eta}(\boldsymbol{x}_f, t)$. Discontinuity of state fields (independent and dependent) on Ω_m across fractures is accommodated by the orientation of a fracture's local coordinate frame. That is, we apply superscripts to refer to either side as $\boldsymbol{n_f} = \boldsymbol{n_f^+} = -\boldsymbol{n_f^-}$. Subsequently, a locally discontinuous state-field such as displacement or pore-pressure will take two-sided values at any point on a fracture. The jump function subsequently defines an implicit fracture aperture (normal gap function),

$$g_N = [\![\boldsymbol{u}]\!] \cdot \boldsymbol{n_f} = (\boldsymbol{u}^+ - \boldsymbol{u}^-) \cdot \boldsymbol{n_f} \quad \text{on} \quad \boldsymbol{x}_f(l) \in \Gamma_f, \, t \geq 0, \tag{1}$$

as well as point-wise tangential slip,

$$g_T = [\![\boldsymbol{u}]\!] \cdot \boldsymbol{\tau_f} = (\boldsymbol{u}^+ - \boldsymbol{u}^-)(\boldsymbol{I} - \boldsymbol{n_f} \otimes \boldsymbol{n_f}) \quad \text{on} \quad \boldsymbol{x}_f(l) \in \Gamma_f, \, t \geq 0. \tag{2}$$

2.2 Governing equations

Within the matrix Ω_m, the continuity of mass and momentum are enforced in the forms,

$$
\begin{cases}
\frac{\partial}{\partial t}\left(\phi^* S_1 \rho_1\right) + \nabla \cdot \left(\rho_1 \boldsymbol{v}_1\right) + q_{1,mf} &= q_1 \\
\frac{\partial}{\partial t}\left(\phi^* S_2 \rho_2\right) + \nabla \cdot \left(\rho_2 \boldsymbol{v}_2\right) + q_{2,mf} &= q_2 \ , \qquad \boldsymbol{x} \in \Omega_m \text{ and } t > 0, \\
\rho_b \frac{\partial^2 \boldsymbol{u}}{\partial t^2} - \nabla \cdot \boldsymbol{\sigma} - \rho_b \boldsymbol{g} &= \boldsymbol{f}
\end{cases}
\tag{3}
$$

where the Lagrange porosity ϕ^* incorporates strain and pore pressure dependent compressibility, ρ_η denotes fluid phase density, ρ_b denotes the overall mass density on a bulk volume basis, $\boldsymbol{v}_\eta$ denotes fluid phase velocity, $q_{\eta,mf}$ represents the phase mass transfer rate from matrix to fracture, q_η denotes phase injection rate from wells, $\boldsymbol{\sigma}$ is the effective stress tensor, $\boldsymbol{f}$ denotes externally-applied body forces, and $\boldsymbol{g}$ denotes the acceleration due to gravity.

Within the fractures Γ_f, $f = 1, \ldots, N_f$, we model one-dimensional multi-phase flow along the tangential coordinate affixed to one of the two tips. Matrix-fracture exchanges of mass are then modeled with a source term. Adopting a lubrication flow limit, the continuity equation for $\eta \in \{1, 2\}$ in fractures is expressed as,

$$
\frac{\partial}{\partial t}\left(g_N S_\eta \rho_\eta\right) - \frac{\partial}{\partial l}\left[g_N^3 \frac{\rho_\eta k_{r,\eta}}{12 \mu_\eta}\left(\frac{\partial P_f}{\partial l} - \rho_f \boldsymbol{g} \cdot \boldsymbol{\tau_f}\right)\right] - q_{\eta,mf} = q_{\eta,f}
\tag{4}
$$

where μ_η is the phase viscosity, $k_{r,\eta}$ denotes phase the relative permeability, and $q_{\eta,f}$ represents phase injection directly into fracture space. Note that Equation 4 is mathematically degenerate in locales where a fracture is closed under contact conditions; i.e., $g_N \equiv 0$. Moreover, in such instances, the independent (fluid pressure and a phase saturation) and dependent (e.g., phase density) variables are undefined. Subsequently, auxiliary constraints are required, and they impose a complementary condition on Equation 4. The auxiliary data and conditions are presented in Section 2.3.

The present model treats the exchange of fluids across the internal matrix and open fracture boundaries as proportional to the local difference between pore pressure and the fracture fluid pressure; i.e.,

$$
q_{\eta,mf} = T_f \frac{\rho_\eta K_{r,\eta}}{\mu_\eta}\left(P^\pm - P_f\right)
$$

Closed fractures may either admit flow across them through the matrix or act as flow barriers.

2.3 Auxiliary data and conditions

For the matrix, the auxiliary data are comprised of boundary and initial conditions. Naturally, the independent state fields $(P(\boldsymbol{x}, 0), S_1(\boldsymbol{x}, 0), \text{ and } \boldsymbol{u}(\boldsymbol{x}, 0))$ may be initialized arbitrarily, subject to compatibility conditions with prescribed boundary conditions to ensure well-posedness. In addition, the initial deformation velocity field $\boldsymbol{v} \equiv \frac{\partial \boldsymbol{u}}{\partial t}$ must be specified. The outer boundary conditions are assumed to be closed to fluid flow, i.e.,

$$
\boldsymbol{v}_\eta \cdot \boldsymbol{n_m} = 0, \qquad \eta \in \{1, 2\} \text{ and } \boldsymbol{x} \in \partial\Omega_m.
$$

Mechanically, we model the outer-boundary as infinite (non-reflecting) by applying absorbing boundary terms. The Lysmer absorbing boundary model (Lysmer & Kuhlemeyer, 1969) is applied by enforcing,

$$
\boldsymbol{\sigma} \cdot \boldsymbol{n_m} = -a_p \bar{\rho}_b \bar{V}_p \frac{\partial \boldsymbol{u}}{\partial t}, \qquad \text{and,}
\tag{5}
$$

$$
\boldsymbol{\sigma} \cdot \left(\boldsymbol{1} - \boldsymbol{n_m} \otimes \boldsymbol{n_m}\right) = -a_s \bar{\rho}_b \bar{V}_s \frac{\partial \boldsymbol{u}}{\partial t}, \qquad \boldsymbol{x} \in \partial\Omega_m.
\tag{6}
$$

In this model, $0 \leq a_p, a_s \leq 1$ are dimensionless parameters to control the degree of absorption, and $\bar{V}_p$ and $\bar{V}_s$ are the average P- and S-wave velocity fields respectively. The velocities are dependent on the independent state fields, and are weighted by mixture density $\bar{\rho}_b$ and mechanical parameters as,

$$\bar{V}_p = \sqrt{\frac{E(1-\nu)}{(1+\nu)(1-2\nu)\bar{\rho}_b}}, \qquad \text{and,} \tag{7}$$

$$\bar{V}_s = \sqrt{\frac{E}{2(1+\nu)\bar{\rho}_b}}, \tag{8}$$

where E is the Young's modulus and ν is the Poisson's ratio.

It is necessary to impose complementarity constraints within fractures to identify and treat open and closed (contact) stick or slip conditions. The augmentation treats the complementarity constraints by introducing local Lagrange multipliers in the normal $\boldsymbol{\lambda}_N$, and tangential $\boldsymbol{\lambda}_T$ directions. These represent the traction on the surface in each direction (Khoei & Nikbakht, 2007; Khoei, 2014). Under open conditions, the local fracture aperture is greater than zero, $g_N > 0$. Subsequently, no additional constraints need to be applied, and the Lagrange multipliers are set equal to zero. Otherwise ($g_N \leq 0$), contact conditions prevail locally, and constraints must be imposed. In turn, these constraints differ under sticking or slipping conditions. In this work, we apply conditions based on the stick-slip theory of friction developed by Curnier (1984). Under the sticking condition $g_T = 0$, the shear slip along the fracture is limited by the frictional forces. Subsequently, according to the Coulomb friction model, $\mu_f \boldsymbol{\lambda}_N - \boldsymbol{\lambda}_T > 0$, and along with the constraint that $\boldsymbol{\lambda}_N > 0$, the Lagrange multipliers may be determined as two additional local degrees of freedom to satisfy these constraints. In the case of sliding conditions ($g_T > 0$) however, and $\boldsymbol{\lambda}_N > 0$ is the only constraint, and the shear traction is set to satisfy $\boldsymbol{\lambda}_T = \mu_f \boldsymbol{\lambda}_N$. These complementarity conditions can be summarized as two sets of Karuch-Kuhn-Tucker conditions for the normal,

$$g_N \geq 0, \boldsymbol{\lambda}_N \geq 0, g_N \boldsymbol{\lambda}_N = 0, \tag{9}$$

and tangential directions,

$$g_T \geq 0, \mu_f \boldsymbol{\lambda}_N - \boldsymbol{\lambda}_T \geq 0, g_T(\mu_f \boldsymbol{\lambda}_N - \boldsymbol{\lambda}_T) = 0. \tag{10}$$

2.3.1 Constitutive relations

Within the matrix, we model phase flow velocity using the multi-phase extension of Darcy's law,

$$\boldsymbol{v}_{\eta,m} = -\bar{\boldsymbol{k}}_{\boldsymbol{m}} \frac{k_{r\eta}}{\mu_\eta} \left(\nabla P + \rho_\eta \boldsymbol{g} \right), \tag{11}$$

where $\bar{\boldsymbol{k}}_{\boldsymbol{m}}$ denotes a spatially varying, diagonal permeability tensor field, and $K_{r,\eta}$ denotes the phase relative permeability relation that is generally a nonlinear function of phase saturation. Empirical thermodynamic correlations are applied to model phase density and viscosity as functions of pore pressure or fracture fluid pressure as appropriate.

The Lagrange porosity ϕ^* integrates deformation dynamics under an assumption of infinitesimal-displacement linear poroelasticity, and is computed as Dean et al. (2006),

$$\phi^* = \phi_0 + \alpha\varepsilon + \frac{1}{M}(P - P_0), \tag{12}$$

where ϕ_0 and P_0 are the reference porosity and pressure, respectively, and α and M are Biot theory parameters, and ε denotes the volumetric strain, which is the trace of

the strain tensor, $\boldsymbol{\varepsilon}$. The mixture density ρ_b is a function of displacement and pressure as the volume-weighted sum,

$$\rho_b = (1 - \phi^*) \rho_s + \phi^* \Sigma_\eta \rho_\eta S_\eta, \tag{13}$$

where ρ_s is the mass density of the solid matrix.

The Biot theory of poroelasticity Biot (1941) is applied, and the effective stress law based on the single-phase theory is modeled as,

$$\boldsymbol{\sigma} = \boldsymbol{\sigma}' - \alpha P \boldsymbol{I}, \tag{14}$$

where $\boldsymbol{\sigma}'$ denoting the effective stress tensor acting between solid grains, and $\boldsymbol{I}$ is the identity tensor. In turn, the effective stress $\boldsymbol{\sigma}'$ is related to displacement via the linear elastic constitutive law,

$$\boldsymbol{\sigma}' = \lambda \left(\nabla \cdot \boldsymbol{u} \right) \boldsymbol{I} + G \left(\nabla^{\mathrm{T}} \boldsymbol{u} + \nabla \boldsymbol{u} \right), \tag{15}$$

where $\lambda > 0$ and $G > 0$ are Lamé coefficients measured experimentally for the matrix skeleton.

Several models may be applied to the evolution of the fracture friction coefficient μ_f. In the computational examples presented, we adopt the linear slip-weakening law Andrews (1976). In this model, the friction factor μ_f is related to the slippage $|g_T|$ as,

$$\mu_f = \begin{cases} \mu_s + \frac{\mu_d - \mu_s}{d_c} |g_T| & |g_T| \leq d_c \\ \\ \mu_d & |g_T| > d_c \end{cases}, \tag{16}$$

where μ_d is a dynamic coefficient parameter, μ_s is a static coefficient parameter, and d_c is a critical distance parameter.

To describe fracture rupture, we define the following terms:

- Reactivation: reactivation occurs when one node on a fracture reaches Coulomb failure.
- Nucleation: in space, once a critical slip length along a fracture is reached (nucleation size), the slipping patch becomes unstable, forming rupture fronts with accelerating slip and spontaneous propagation of elastodynamic rupture. Thus, a rapid increase in slip rate and area are observed. The theoretical nucleation size for a slip-weakening friction model can be estimated from the properties of the given field. Following Jin and Zoback (2018), this is obtained as,

$$L_c = \frac{E d_c}{2(1 + \nu)(1 - \nu)(\mu_s - \mu_d)\sigma_n}, \tag{17}$$

where σ_n is the normal stress at the onset of Coulomb failure.

The proposed model extends an established quasi-static numerical scheme and solution methodology Ren et al. (2018); Ren and Younis (2021a) to incorporate fracture contact and slip dynamics as well as inertial poromechanics. The base quasi-static numerical method is first briefly described, and the reader is referred to Ren et al. (2018) and Ren and Younis (2021a) for further details. Following the review, we then develop two extensions to the method. The first extension incorporates closed and stick and slip constraints on fractures, and the second extension pertains to incorporating inertial effects in the coupled poromechanics.

2.4 Review of the base quasi-static numerical model

The model applies an independent Cartesian mesh to approximate Ω_m and a one-dimensional Piecewise Linear Complex (PLC) mesh to approximate fractures Γ_f.

Generally, the fracture mesh (choice of segmentation of fractures) can be independent of the choice of matrix mesh. While this feature may be desirable in practice, in the computational examples presented, we select fracture segments to conform to the edges of the matrix mesh cells which they intersect. Mixed discretizations are applied to the mass and momentum conservation equations. The flow equations on the matrix and fractures are approximated using a finite-volume approximation (Lee et al. (2001) and Li and Lee (2008)). In contrast, the poromechanical equations are approximated using an extended finite element method XFEM (Moës et al. (1999)). A stabilized interpolation of unknowns ensures complete coupling across the two systems. Staggering variables enable this; pressure and saturation unknowns are matrix cell and fracture segment centered, whereas displacement variables are located at mesh vertices. We apply interpolation schemes that guarantee the Ladyzhenskaya-Babuska-Brezzi (LBB) stability conditions. This mixed discretization approach improves the approximation of sharp saturation fronts in multiphase flow.
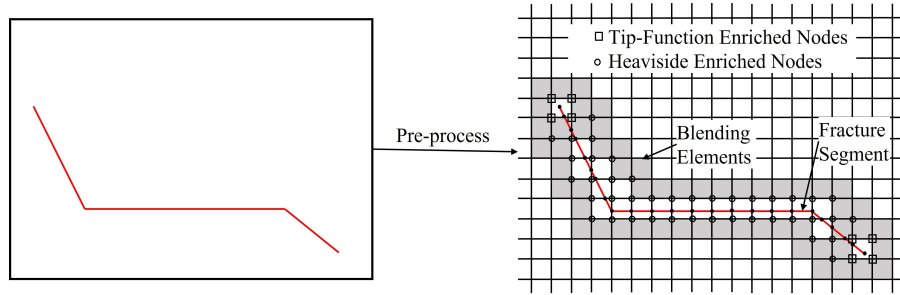

Figure 4: Illustration of the geometry and finite-element enrichment of nodes and elements in the vicinity of an embedded fracture.

As illustrated in Figure 4, XFEM applies Heaviside and tip enrichment to nodes in the vicinity of fracture segments. This enrichment ensures accurate approximation of discontinuity in the displacement field as well as singularity at fracture tips. While the approach of Ren et al. (2018) accommodates fracture segment intersections and that of Ren and Younis (2021a, 2021c, 2021b) additionally accommodates fluid-driven tip propagation, both of these effects are neglected in the present work. The proposed work augments this enrichment with numerical constraint terms to model the fracture contact and stick-slip dynamics described in Section 2.3.

We apply a projection Embedded Discrete Fracture and Matrix (pEDFM) finite volume approximation (Jiang and Younis (2016b); Ţene et al. (2017)) to the flow and transport equations within both the matrix and fracture segments. As illustrated in Figure 5, the matrix cell- and fracture segment-centered method introduces transmissibility connections that carry material flux. The transmissibility weights are functions of the local geometry and are subsequently computed offline in a preprocessing step. Closed fracture segments (Figures 5c and 5d) result in a degenerate mass conservation residual for that segment. Subsequently, the associated degrees of freedom and connections must be annihilated or redistributed to the matrix cells. These alterations must be implemented dynamically as the opening of segments is dictated by the evolution of the underlying poro-hydro-mechanical process.

2.5 Extension to incorporate fracture contact and slip conditions

Introducing the variational form of the displacement field $\delta \boldsymbol{u}(\boldsymbol{x}, t)$ and the associated variational strain tensor $\delta \boldsymbol{\varepsilon} := \nabla^{sym} \delta \boldsymbol{u}$, the weak form of the momentum

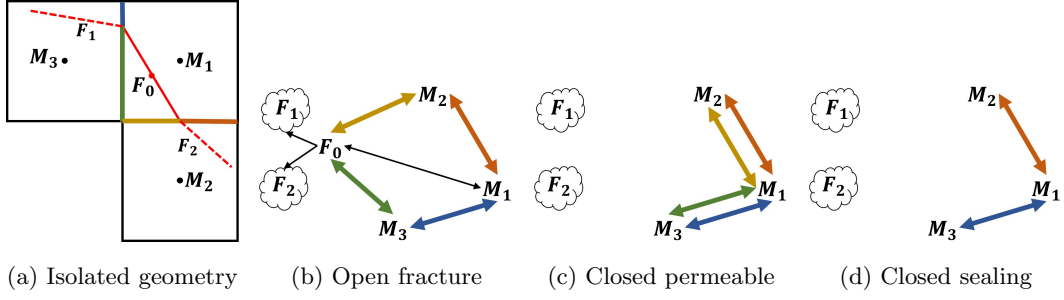(a) Isolated geometry   (b) Open fracture   (c) Closed permeable   (d) Closed sealing

Figure 5: Illustration of the geometry and finite volume connectivity of a hypothetical cell with an embedded fracture under various conditions: (a) geometry and projection areas for a fracture segment with unknowns centered at F_0, embedded in cell with unknowns centered at M_1; (b) through (d) connectivity between segments and cells under open, closed but transmissible, and closed sealing conditions.

balance in Equation 3 is,

$$\int_{\Omega_m} \delta\boldsymbol{u} \cdot (\rho_b \ddot{\boldsymbol{u}})\, d\Omega + \int_{\Omega_m} \delta\boldsymbol{\varepsilon} \cdot \boldsymbol{\sigma} d\Omega - \int_{\Omega_m} \delta\boldsymbol{u} \cdot \boldsymbol{f} d\Omega = \int_{\Gamma_t} \delta\boldsymbol{u} \cdot \bar{\boldsymbol{t}} d\Gamma + \boldsymbol{W_f}, \qquad (18)$$

where $\boldsymbol{W_f}$ denotes the externally-applied virtual work due to the internal fractures, and $\bar{\boldsymbol{t}}$ denotes the traction forces applied to the traction (Neumman) boundary Γ_t on outer boundary of Ω_m. The second term on the left-hand-side of Equation 18 captures the action of the total stress, and through the Biot model in Equation 14 expands to,

$$\int_{\Omega_m} \delta\boldsymbol{\varepsilon} \cdot \boldsymbol{\sigma} d\Omega = \int_{\Omega_m} \delta\boldsymbol{\varepsilon} : \boldsymbol{D} : \boldsymbol{\varepsilon} d\Omega - \int_{\Omega_m} \delta\boldsymbol{\varepsilon} : (\alpha P \boldsymbol{I}) d\Omega, \qquad (19)$$

where $\boldsymbol{D}$ is the elasticity tensor of the solid skeleton, and P is the matrix pore pressure. In Ren and Younis (2018, 2021a), fractures are assumed to be open exclusively. Subsequently, the force boundary condition on fractures is modeled as,

$$\boldsymbol{W}_{n,f}^{open} = \int_{\Gamma_f} P_f \delta g_N \, d\Gamma, \qquad (20)$$

which posits that the fluid pressure within the fractures P_f leads to the sole surface force that is applied onto the matrix. We extend this model to account for changing conditions to closed fractures under either sticking or sliding conditions. A Lagrange Multiplier approach is applied to impose these constraints exactly. These conditions are listed in Equations 9 and 10 for the normal and tangential directions respectively. Further degrees of freedom are added for the contact pressure in the normal direction $\boldsymbol{\lambda}_N$ and the tangential traction $\boldsymbol{\lambda}_T$. The Lagrange multipliers are aligned as the independent unknowns of additional algebraic equations, and they also contribute to alternative forms of $\boldsymbol{W}_f$ in the variational form of the momentum equations. These are developed next.

Under closed conditions, the contribution of the normal traction $\boldsymbol{\lambda}_N$ to the balance of virtual work becomes,

$$\boldsymbol{W}_{n,f}^{closed} = \int_{\Gamma_f} \boldsymbol{\lambda}_N \delta g_N \, d\Gamma. \qquad (21)$$

The tangential virtual work term will depend on whether the segments are in a sticking or slipping state. Under sticking conditions, the term is,

$$\boldsymbol{W}_{st,f}^{closed} = \int_{\Gamma_f} \boldsymbol{\lambda}_T \delta g_T \, d\Gamma. \qquad (22)$$

Under sliding conditions however, a suitable friction model must be enforced. The Coulomb friction model relates the friction coefficient and contact force as,

$$\boldsymbol{W}_{sl,f}^{closed} = \int_{\Gamma_f} sign(\boldsymbol{g}_T)\mu_f \parallel \boldsymbol{\lambda}_N \parallel \delta\boldsymbol{g}_T \, d\Gamma. \tag{23}$$

In summary, the virtual work term for internal (embedded) fractures is,

$$\boldsymbol{W}_f = \begin{cases} \boldsymbol{W}_{n,f}^{open} & g_N > 0 \\ \boldsymbol{W}_{n,f}^{closed} + \boldsymbol{W}_{st,f}^{closed} & g_N = g_T = 0 \\ \boldsymbol{W}_{n,f}^{closed} + \boldsymbol{W}_{sl,f}^{closed} & g_N = 0, \ \|g_T\| > 0 \end{cases}. \tag{24}$$

The additional variational equations with which the multipliers are aligned require numerical stabilization. This is necessary due to the failure of the discrete subspace to satisfy the Ladyzhenskaya–Babuška–Brezzi (LBB) stability condition. Instability manifests in spurious oscillations in the normal and tangential tractions. We apply the Pressure Projection Polynomial (PPP) method that adds a stabilization term to the normal and tangential constraint equations, penalizing the deficiency in displacement and contact traction approximation (F. Liu & Borja, 2010). The stabilized normal contact constraint equation is,

$$\int_{\Gamma_f} \delta\boldsymbol{\lambda}_N g_N \, d\Gamma - \int_{\Gamma_f} \frac{\tau}{2M}(\hat{\boldsymbol{N}} - \Pi\hat{\boldsymbol{N}})^T(\boldsymbol{\lambda}_N - \Pi\boldsymbol{\lambda}_N) \, d\Gamma = 0, \tag{25}$$

and the tangential equation,

$$\int_{\Gamma_f} \delta\boldsymbol{\lambda}_T g_T \, d\Gamma - \int_{\Gamma_f} \frac{\tau}{2M}(\hat{\boldsymbol{N}} - \Pi\hat{\boldsymbol{N}})^T(\boldsymbol{\lambda}_T - \Pi\boldsymbol{\lambda}_T) \, d\Gamma = 0, \tag{26}$$

where M is the volume modulus of the bulk material and is equal to Young's modulus of elasticity, τ is a normalized stabilization parameter, and Π is a projection operator that acts on the interface shape function $\hat{\boldsymbol{N}}$ as follows,

$$\Pi\hat{\boldsymbol{N}} = (\frac{1}{2}, \frac{1}{2}). \tag{27}$$

With the variational problem in hand, an XFEM discretization is applied as presented in Ren et al. (2018); Han et al. (2020); Ren and Younis (2021a). Introducing dot notation to denote temporal derivatives, the spatially semi-discrete matrix form of the resulting residual system is of the form,

$$\begin{cases} \boldsymbol{M}\ddot{\boldsymbol{u}} + \boldsymbol{C}\dot{\boldsymbol{u}} + \boldsymbol{K}\boldsymbol{u} + \boldsymbol{G_N}\boldsymbol{\lambda}_N + \boldsymbol{G_T}\boldsymbol{\lambda}_T & = \boldsymbol{F} \\ \boldsymbol{G_N^T}\boldsymbol{u} + \boldsymbol{S}\boldsymbol{\lambda}_N & = 0 \\ \boldsymbol{G_T^T}\boldsymbol{u} + \boldsymbol{S}\boldsymbol{\lambda}_T & = 0 \end{cases}, \tag{28}$$

where $\boldsymbol{M}$ is the global mass matrix, $\boldsymbol{C}$ is the global damping matrix, $\boldsymbol{K}$ is the global stiffness matrix, $\boldsymbol{F}$ is the externally applied load which may be time-dependent, $\boldsymbol{G_N}$ is the normal traction constraint on fractures, $\boldsymbol{G_T}$ is the tangential counterpart, and $\boldsymbol{S}$ is the stabilization matrix. In terms of the shape function matrix $\boldsymbol{N}$, the shape function of interfacial elements $\hat{\boldsymbol{N}}$, and the displacement-strain transformation matrix

B these coeffiencts are expanded as,

$$
\begin{aligned}
\boldsymbol{M} &= \iint_{\Omega_m} \boldsymbol{N}^{\mathrm{T}} \rho_b \boldsymbol{N} d\Omega, && \text{(inertial term)} \\
\boldsymbol{K} &= \iint_{\Omega_m} \boldsymbol{B}^{\mathrm{T}} D \boldsymbol{B} d\Omega, && \text{(internal force term)} \\
\boldsymbol{F} &= \iint_{\Omega_m} \boldsymbol{B}^T (\alpha \boldsymbol{P} \boldsymbol{I}) d\Omega + \int_{\Gamma_t} \boldsymbol{N} \cdot \bar{\boldsymbol{t}} d\Gamma, && \text{(external force term)} \\
\boldsymbol{G}_N &= \int_{\Gamma_f} \llbracket \boldsymbol{N} \rrbracket^T \boldsymbol{n}_f \hat{\boldsymbol{N}} \, d\Gamma, && \text{(normal contact force term)} \\
\boldsymbol{G_T} &= \int_{\Gamma_f} \llbracket \boldsymbol{N} \rrbracket^T \boldsymbol{\tau}_f \hat{\boldsymbol{N}} \, d\Gamma, && \text{(tangential contact force term)} \\
\boldsymbol{S} &= - \int_{\Gamma_f} \frac{\tau}{2M} (\hat{\boldsymbol{N}} - \Pi \hat{\boldsymbol{N}})^T (\hat{\boldsymbol{N}} - \Pi \hat{\boldsymbol{N}}) \, d\Gamma, && \text{(stabilization term)}
\end{aligned}
\tag{29}
$$

The global damping matrix $\boldsymbol{C}$ is modeled as a combination of Rayleigh damping and and equivalent damping operator to model absorbing (non-reflecting) boundaries. That is,

$$
\boldsymbol{C} = \boldsymbol{C}_R + \boldsymbol{C}_A,
\tag{30}
$$

where the Rayleigh damping matrix $\boldsymbol{C}_R$ is introduced to suppress oscillations under high frequency deformation. The damping is the classical mass and stiffness proportionate matrix (M. Liu & Gorman, 1995) and is,

$$
\boldsymbol{C}_R = a\boldsymbol{M} + b\boldsymbol{K}.
\tag{31}
$$

a and b are the Rayleigh damping coefficients. The equivalent damping matrix $\boldsymbol{C}_A$ is derived from the absorbing boundary conditions and is assembled as,

$$
\boldsymbol{C}_A = \int_{\Gamma} \boldsymbol{N}^T \bar{\rho}_b \boldsymbol{V} \boldsymbol{N} d\Gamma,
\tag{32}
$$

The natural material velocity $\boldsymbol{V}$ is given as,

$$
\boldsymbol{V} =
\begin{cases}
\begin{bmatrix} a_p \bar{V}_p & 0 \\ 0 & a_s \bar{V}_s \end{bmatrix}, & \mathit{if}\ \boldsymbol{n}_\Gamma \parallel x \\[2em]
\begin{bmatrix} a_s \bar{V}_s & 0 \\ 0 & a_p \bar{V}_p \end{bmatrix}. & \mathit{if}\ \boldsymbol{n}_\Gamma \parallel y
\end{cases}
\tag{33}
$$

2.6 Temporal discretization

The second extension to the base model is a temporal discrete approximation of the inertial terms. We apply an implicit method derived from the generalized Newmark GN22 scheme (Newmark, 1959). The scheme offers unconditional stability and second-order accuracy with appropriate parameters. At a given time-step number $n = 1, 2, \ldots$, the state approximations at t^{n-1} are available, and the objective is to solve the coupled algebraic for $t^n = t^{n-1} + \Delta t$. In Equation 28, all independent variables (both for flow and mechanics) are taken at the target time level (fully-implicit). The velocity $\dot{\boldsymbol{u}}$ is approximated as,

$$
\dot{\boldsymbol{u}} \approx \frac{\delta}{\beta \Delta t} \left(\boldsymbol{u}^n - \boldsymbol{u}^{n-1} \right) + \left(1 - \frac{\delta}{\beta} \right) \dot{\boldsymbol{u}}^{n-1} + \left(1 - \frac{\delta}{2\beta} \right) \ddot{\boldsymbol{u}}^{n-1} \Delta t,
\tag{34}
$$

and the acceleration $\ddot{\boldsymbol{u}}$ as,

$$
\ddot{\boldsymbol{u}} \approx \frac{1}{\beta \Delta t^2} \left(\boldsymbol{u}^n - \boldsymbol{u}^{n-1} \right) - \frac{1}{\beta \Delta t} \dot{\boldsymbol{u}}^{n-1} + (1 - \frac{1}{2\beta}) \ddot{\boldsymbol{u}}^{n-1},
\tag{35}
$$

where β and δ are user-defined parameters. A well-established numerical artifact of the temporal discretization of wave equations is oscillatory error modes at high frequency (see for example, Appendix A). A common numerical treatment is to apply dissipate damping to remove such high-frequency modal components. In terms of the Newmark method, a choice of $\delta > 0.5$ introduces such high-frequency dissipation, and by further selecting $\beta = 0.25(0.5 + \delta)^2$, this dissipation may be maximized. On the other hand, a choice of $\delta \neq 0.5$ results in a drop to first-order accuracy (Mathews & Fink, 2004; Géradin & Rixen, 2014). For this work, we select $\delta = 0.5$ and $\beta = 0.25$, and to introduce sufficient dissipation while retaining asymptotic accuracy, we utilize Rayleigh Damping (Equation 31).

2.7 Fully-coupled, implicit, and monolithic solution procedure

The independent discrete fields are the matrix cell pore pressure $\boldsymbol{P}$ and phase saturation $\boldsymbol{S}$, open fracture segment fluid pressure $\boldsymbol{P}_f$ and saturation $\boldsymbol{S}_f$, the displacement vector field $\boldsymbol{u}$, and the Lagrange Multipliers ($\boldsymbol{\lambda}$). These unknowns are aligned with the pEDFM discrete mass conservation equations in matrix cells and fracture segments, along with Equations 28 respectively. The coupled nonlinear system of algebraic equations is solved at each time-step using an Inexact-Newton method. In this work, we lag the determination of the contact and slip conditions on fracture segments by one time-step. During the nonlinear solution process, we do not allow the fracture segment status to change until convergence. This generally improves nonlinear convergence by eliminating the local non-differentiability in the residual due to changing constraint equations. Otherwise, a common artifact is the occurrence of Newton k-cycles $k > 1$ where a segment may oscillate between sticking and slipping conditions across k consecutive iterations. This solution process is listed in Algorithm 1.

Initialize guess for the primary variables $\boldsymbol{V}^n = (\boldsymbol{P}, \boldsymbol{S}, \boldsymbol{u}, \boldsymbol{\lambda}_N, \boldsymbol{\lambda}_T)^{n-1}$
while *not converged* **do**
  Assemble the Jacobian matrix $J(\boldsymbol{V}^n, \boldsymbol{V}^{n-1}, \Delta t)$
  Calculate residual $R(\boldsymbol{V}^n, \boldsymbol{V}^{n-1}, \Delta t)$
  Approximately solve $\delta \boldsymbol{V}$ from equation $J^{-1}\delta \boldsymbol{V} = -\boldsymbol{R}$
  Update primary variables $\boldsymbol{V}^n = \boldsymbol{V}^{n-1} + \lambda\delta \boldsymbol{V}$ with $0 < \lambda \leq 1$
  Update $\dot{\boldsymbol{u}}^n, \ddot{\boldsymbol{u}}^n$ using 34 and 35
end
For each fracture segment, check contact conditions:
if $\boldsymbol{\lambda}_T^n < \mu_f \parallel \boldsymbol{\lambda}_N^n \parallel$ **then**
  Designate segment to a sticking condition
else
  Designate segment in a sliding condition, and set $\boldsymbol{\lambda}_T^n = sign(g_T)\mu_f \parallel \boldsymbol{\lambda}_N^n \parallel$
end
Algorithm 1: Monolithic Inexact-Newton solution procedure for a time step

3 Proposed Adaptive Time-Step Control

The proposed seamless model provides estimates for the displacement, fracture stress, and velocity fields at each time step. This allows for the design of a hybrid time step control strategy that combines discretization error, time to rupture, and slip velocity considerations simultaneously with little computational overhead. At any given point in a simulation, the underlying process will dictate which of these considerations becomes the limiting factor for an upcoming time step size. For instance, in pre-nucleation stages, the local time discretization error and the earliest time for a fracture node to experience rupture are likely to compete as the limiting factors. Progressing from rupture towards nucleation, the latter factor will tend to dominate.

After nucleation, the slip rate increases rapidly, and becomes the chief limiting factor. Approaching arrest, this effect diminishes, and gives way to the less restrictive error criteria, allowing for larger time step sizes.

Before assembling these three criteria into an automatic time step control strategy, we develop the individual criteria. All criteria require prescribed maximum and minimum step sizes ($\Delta t_{max} > \Delta t_{min} > 0$). The maximum step size may be related to other considerations such as changing well controls or the desired accuracy of flow variables, for example. The minimum step size can be related to the fastest characteristic slip velocity scaled by the fracture geometry.

3.1 Discretization error time step control

An *a posteriori* local discretization error estimate and optimal step size selection method are proposed by Mayr et al. (2018) for the Newmark scheme applied to fluid-structure interaction problems. This approach is extended and applied to the current context.

Given a time step solution, the method provides an assessment of whether or not an error constraint is satisfied, as well as a proposed time step size. If the error constraint is violated, the time step is repeated using a smaller proposed size. Otherwise, the proposed step size may be larger than the original, and it is used for the next solution step.

At simulation time t^n, the goal is determine a step size $\Delta t^n_{error} \in [\Delta t_{max}, \Delta t_{min}]$ so that the local error $e^{n+1} = \left\| \boldsymbol{u}^{n+1} - \boldsymbol{u}\left(t^{n+1}\right) \right\|_2$ at the new time $t^{n+1} = t^n + \Delta t^n_{error}$ is less than prescribed tolerance $\varepsilon_1 > 0$. The test for this condition uses the computed estimate,

$$e^{n+1} \approx \left\| (\beta - \frac{1}{6})\Delta t^{n,2}(\ddot{\boldsymbol{u}}^{n+1} - \ddot{\boldsymbol{u}}^n) \right\|_2, \tag{36}$$

where $\beta = 0.25$ is the Newmark parameter, and $\ddot{\boldsymbol{u}}$ is the computed acceleration using the Newmark scheme. In addition to this *a posteriori* test, an optimized scaling factor is computed to increase or decrease the time step size in order to satisfy the constraint. This scaling factor is computed as,

$$k^* = \sqrt{\frac{\varepsilon_1}{e^{n+1}}}. \tag{37}$$

The following prescribed parameters are then required to compute the proposed step size: $0 < k_{min} < 1$ is a minimum allowed scaling ratio by which to decrease step size, $1 < k_{max}$ is a maximum allowed scaling ratio to increase step size, and $0 < k_s < 1$ is a safety factor to reduce the need for frequent time step repetitions. Given these parameters, the proposed step size is computed as,

$$\Delta t^* = \min\left(\Delta t_{max}, \max\left(\min\left(k_{max}, \max\left(k_{min}, k_s k^*\right)\right)\Delta t_n, \Delta t_{min}\right)\right). \tag{38}$$

Finally, to further reduce the likelihood of overshoot, the proposed step size can be taken as a convex combination with previous time-step sizes, i.e.,

$$\Delta t^n_{error} = \gamma_n \Delta t^* + \Sigma_{m=1}^{M} \gamma_{n-m} \Delta t^{n-m}_{error}, \tag{39}$$

where γ_i are prescribed weights that satisfy $\Sigma_{m=0}^{M} \gamma_{n-m} = 1$, and $M \geq 0$ is a prescribed number of previous steps to utilize.

3.2 Earliest time to Coulomb failure

Jin and Zoback (2018) define a Coulomb Failure Criterion (CFF) to indicate whether a location on a fault is undergoing slip. In the continuous sense, the CFF is

defined as,

$$CFF(x,t) = \|\boldsymbol{\sigma} \cdot \boldsymbol{\tau}_f\| - \mu_s \|\boldsymbol{\sigma} \cdot \boldsymbol{n}_f\|, \tag{40}$$

where $\boldsymbol{\sigma} \cdot \boldsymbol{\tau}_f$ is the shear component of stress along the fracture and $\boldsymbol{\sigma} \cdot \boldsymbol{n}_f$ is the normal component of stress. A negative CFF indicates a sticking condition, whereas a positive value indicates slip.

A numerical counterpart to the CFF may be computed at each fracture location $i = 1, \ldots, N_f$. Using the Lagrange Multipliers, the numerical estimates at these locations are,

$$C_i^n = \|\lambda_{T,i}^n\| - \mu_s \|\lambda_{N,i}^n\|. \tag{41}$$

At a fracture location for which C_i^n is negative, we estimate the time step size $\Delta t_{cff,i}^n > 0$ for the point to reach Coulomb failure (i.e., for which $C_i^{n+1} = 0$). This estimate is based on extrapolation from a local model that is fitted to previous solution states. In particular, we propose two alternative models: a linear model based on the current and previous time step solutions, and a Legendre polynomial of minimal degree less than two. In either case, the earliest time step for Coulomb failure is taken as,

$$\Delta t_{cff}^n = \min_{1 \le i \le N_f} \Delta t_{cff,i}^n. \tag{42}$$

The polynomial model memory storage requirement is double that of the linear model. While in cases for which the previous numerical CFF values are colinear, it produces an equivalent estimate to that of the linear model, in other cases, it will not. Example scenarios are illustrated in Figure 6, and the particulars of either model are developed next.

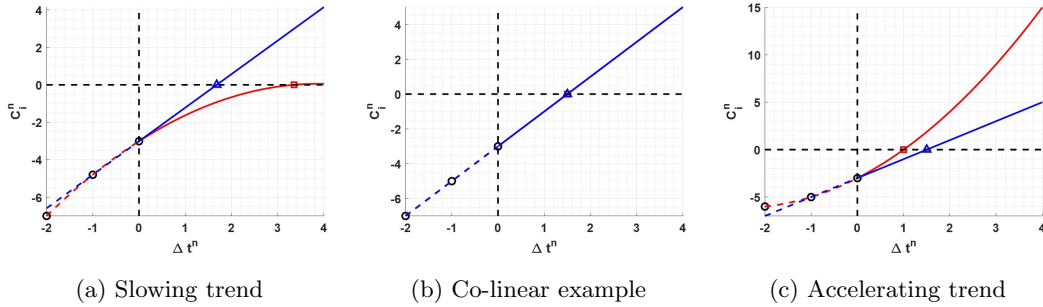(a) Slowing trend   (b) Co-linear example   (c) Accelerating trend

Figure 6: Illustrations of CFF time step size prediction for three scenarios. Dashed and solid lines represent interpolation and extrapolation, respectively, using the linear (blue) and polynomial (red) models. ◯ is a computed previous state, △ is the linear prediction, and □ is the polynomial prediction.

3.2.1 Linear extrapolation

As illustrated in Figure 6, for $n > 0$ the computed CFF values from previous iterations may be used in a secant rule as,

$$\Delta t_{cff,i}^n = \begin{cases} \dfrac{C_i^n}{C_i^{n-1} - C_i^n} \Delta t_{n-1} & \text{if } 0 > C_i^n > C_i^{n-1} \\ \Delta t_{max} & \text{otherwise} \end{cases} . \tag{43}$$

3.2.2 Polynomial extrapolation

For steps $n > 1$, the previous three state solutions are used to construct a local minimal-degree polynomial model for the discrete CFF variation with Δt^n and the nodal time for Coulomb failure is extrapolated. In particular, for fracture element i, and given the computed values C_i^{n-2}, C_i^{n-1}, and C_i^n corresponding to time steps Δt^{n-2} and Δt^{n-1}, the fitted Lagrange polynomial is,

$$P_i\left(\Delta t^n\right) = \alpha_0 C_i^n - \alpha_1 C_i^{n-1} + \alpha_2 C_i^{n-2}, \tag{44}$$

where the coefficients are,

$$\alpha_0 = \frac{\left(\Delta t^n + \Delta t^{n-1} + \Delta t^{n-2}\right)\left(\Delta t^n + \Delta t^{n-1}\right)}{\Delta t^{n-1}\left(\Delta t^{n-1} + \Delta t^{n-2}\right)} \tag{45}$$

$$\alpha_1 = \frac{\Delta t^n\left(\Delta t^n + \Delta t^{n-1} + \Delta t^{n-2}\right)}{\Delta t^{n-1}\Delta t^{n-2}} \tag{46}$$

$$\alpha_2 = \frac{\Delta t^n\left(\Delta t^n + \Delta t^{n-1}\right)}{\Delta t^{n-2}\left(\Delta t^{n-1} + \Delta t^{n-2}\right)} \tag{47}$$

An analysis for the minimal positive and real root of this polynomial yields a computational estimate for the target time step to achieve nodal Coulomb failure. We define the following terms,

$$a_i = \Delta t^{n-2} C_i^n - \left(\Delta t^{n-1} + \Delta t^{n-2}\right) C_i^{n-1} + \Delta t^{n-1} C_i^{n-2}, \tag{48}$$

$$b_i = \Delta t^{n-2}\left(\Delta t^{n-2} + 2\Delta t^{n-1}\right) C_i^n - \left(\Delta t^{n-1} + \Delta t^{n-2}\right)^2 C_i^{n-1} + \left(\Delta t^{n-1}\right)^2 C_i^{n-2}, \tag{49}$$

$$c_i = \Delta t^{n-1}\Delta t^{n-2}\left(\Delta t^{n-2} + \Delta t^{n-1}\right) C_i^n, \tag{50}$$

$$d_i = b_i^2 - 4a_i c_i, \tag{51}$$

$$r_{1,i} = -\frac{b + \sqrt{d_i}}{2a_i}, \text{ and,} \tag{52}$$

$$r_{2,i} = -\frac{b - \sqrt{d_i}}{2a_i}. \tag{53}$$

Subsequently, the estimated earliest time to Coulomb failure is,

$$\Delta t_{cff,i}^n = \begin{cases} -\frac{c_i}{b_i} & \text{if } a_i = 0, b_i > 0, \text{ and } c_i < 0 \\ \sqrt{-\frac{c_i}{a_i}} & \text{if } a_i > 0, b_i = 0, \text{ and } c_i < 0 \\ -\frac{2c_i}{b_i} & \text{if } a_i = \frac{b_i^2}{4c_i}, b_i > 0, \text{ and } c_i < 0 \\ r_{1,i} & \text{if } d_i > 0, a_i < 0, 0 < b_i < \sqrt{d_i}, \text{ and } c_i < 0 \\ r_{2,i} & \text{if } d_i > 0, a_i < 0, \sqrt{d_i} < b_i, \text{ and } c_i < 0 \\ r_{1,i} & \text{if } d_i > 0, a_i > 0, b_i < -\sqrt{d_i}, \text{ and } c_i < 0 \\ r_{2,i} & \text{if } d_i > 0, a_i > 0, -\sqrt{d_i} < b_i < \sqrt{d_i}, \text{ and } c_i < 0 \\ \Delta t_{max} & \text{otherwise} \end{cases} \tag{54}$$

3.3 Slip rate-based time step

A rapid increase in tangential slip rate at fault locations can serve as an indicator of the nucleation of dynamic rupture. Under quasi-static slip, the slip rate is relatively much smaller than that after nucleation. Equation 2 provides a definition for slip, and assuming that the fracture curvature remains constant, the rate of slip is subsequently,

$$\dot{g}_T = \left(\dot{u}^+ - \dot{u}^-\right)\left(I - n_f \otimes n_f\right) \tag{55}$$

Computational estimates of slip rate at fracture locations require knowledge of the instantaneous one-sided velocity fields on either side of the fracture. In stitched models

that apply a quasi-static assumption prior to rupture, velocity estimates may only be obtained by extrapolation from previous state solutions. For example, at a fracture location i and time step n, the instantaneous slip rate in a stitched model may be approximated using an explicit first-order model as,

$$\dot{g}_{i,T}^n = \frac{1}{\Delta t^{n-1}} \left(\boldsymbol{u}_i^{+,n} - \boldsymbol{u}_i^{+,n-1} - \boldsymbol{u}_i^{-,n} - \boldsymbol{u}_i^{-,n-1} \right) \left(\boldsymbol{I} - \boldsymbol{n_{f,i}} \otimes \boldsymbol{n_{f,i}} \right) \tag{56}$$

The explicit estimate is prone to missing a sudden transition during rupture. Moreover, it is particularly sensitive to the time step sizes used during the quasi-static process. In the proposed seamless model, the estimates are obtained using the Newmark velocity state directly, and without the need for extrapolation, i.e.,

$$\dot{g}_{i,T}^n = \left(\dot{\boldsymbol{u}}_i^{+,n} - \dot{\boldsymbol{u}}_i^{-,n} \right) \left(\boldsymbol{I} - \boldsymbol{n_{f,i}} \otimes \boldsymbol{n_{f,i}} \right) \tag{57}$$

Introducing a prescribed safety factor $0 < \eta \leq 1$, the proposed time step size to control slip-rate is obtained for each fracture node as,

$$\Delta t_{i,slip}^n = \min \left(\Delta t_{max}, \eta \frac{d_c}{\dot{g}_{T,i}^n} \right), \tag{58}$$

and globally, as,

$$\Delta t_{slip}^n = \min_{1 \leq i \leq N_f} \Delta t_{slip,i}^n. \tag{59}$$

3.4 Transition from dynamic rupture to arrest

To efficiently accommodate a transition from dynamic rupture to arrest as well as the possibility of multiple cycles of such transitions, we incorporate an additional solution state indicator variable $I^n \in \{0, 1\}$ that takes a value of one if any fractures are undergoing dynamic rupture and zero otherwise. Following a transition over a time step from a value of one to zero, a single quasi-static solution is performed to resolve small transients, and allow for a rapid growth of the time step size. Suppose that at time step $n > 0$ the model was in a dynamic rupture state ($I^{n-1} = 1$), and that the computed maximum slip speed drops below a prescribed threshold v_{thresh}, i.e.,

$$g_{T,\max}^{n+1} < v_{min}. \tag{60}$$

Then the state indicator switches ($I^{n-1} = 0$), and a single quasi-static solution step is performed (by neglecting the inertial terms). Subsequently, small transients reach equilibrium, thereby allowing a rapid growth of the time step size in subsequent steps.

3.5 Hybrid time step selection algorithm

The proposed time steps obtained from each of the three considerations are combined into an adaptive control method for temporal advancement. Since the consideration for error control relies on *a posteriori* computation, it must be implemented using a *try and adapt* strategy.

The time advancement algorithm is listed in Algorithm 2. Note that the slipping patch size of a given fracture is the total length of all contiguous elements along a fracture that are experiencing slip. Furthermore, $v_{min} \in]0, v_{thresh}[$ is a prescribed tolerance for the smallest allowable slip rate under dynamic rupture conditions.

4 Computational Examples

The proposed extensions are implemented in an in-house implementation written in the C++ programming language that utilizes the Automatically Differentiable

Input: $\boldsymbol{V}^0 = (\boldsymbol{u}^0, \dot{\boldsymbol{u}}^0, \boldsymbol{p}^0, \boldsymbol{S}^0, \boldsymbol{\lambda}_N^0, \boldsymbol{\lambda}_T^0)$, $I^0 = 0$, and assuming sticking conditions.
Assign $n \leftarrow 0$, $t^0 \leftarrow 0$, $L^0 \leftarrow 0$, and $\Delta t^0 \leftarrow \Delta t_{min}$.
while $t^{n+1} < t_{final}$ **do**

    Apply Algorithm 1 to solve time step for V^{n+1}.
    Estimate local error e^n, and proposed Δt_{error}^n.
    if $e^n > \varepsilon_1$ **then**
        | Cut time step size and repeat, $\Delta t_n \leftarrow \Delta t_{error}^n$
    else
        if $I^n = 0$ **then**
            Compute slipping patch length, $L^{n+1} \leftarrow \max_{f=1,\dots,N_f} L_f^{n+1}$
            if $L^{n+1} \geq L_c$ **then**
                $I^{n+1} \leftarrow 1$
                $\Delta t^{n+1} \leftarrow \Delta t_{slip}^{n+1}$
            else
                $I^{n+1} \leftarrow 0$
                $\Delta t^{n+1} \leftarrow \min\left(\Delta t_{slip}^{n+1}, \Delta t_{error}^{n+1}, \Delta t_{CFF}^{n+1}\right)$
            end
        else
            if $g_{T,\max}^{n+1} < v_{min}$ **then**
                $I^{n+1} \leftarrow 0$
                Solve a quasi-static step with Δt_{min}
                $\Delta t^{n+1} \leftarrow \min\left(\Delta t_{slip}^{n+1}, \Delta t_{error}^{n+1}, \Delta t_{CFF}^{n+1}\right)$
            else
                $I^{n+1} \leftarrow 1$
                $\Delta t^{n+1} \leftarrow \Delta t_{slip}^{n+1}$
            end
        end
        Advance time step counter, $n \leftarrow n + 1$
        $\Delta t^n \leftarrow \min\left(\Delta t^n, t_{final} - t^n\right)$
    end
end

Algorithm 2: Proposed adaptive time step advancement algorithm

Expression Templates (ADETL) library (R. Younis & Aziz, 2007; R. M. Younis, 2011; R. M. Younis & Tchelepi, 2012). The implementation aspects of the fluid flow in-house model are described in (Jiang & Younis, 2015b, 2015a, 2016b, 2016a, 2017), and the mechanical treatments in (Ren et al., 2016b, 2016a, 2018; Xu et al., 2021; Han et al., 2020) A direct sparse linear solver is used for validation examples, and a preconditioned fGMRES indirect method otherwise. Appendix A presents validation results characterizing the correctness and accuracy of the implemented temporal discretization. Appendix B presents a validation study of the implemented fracture contact and slip condition treatments.

Two synthetic cases are constructed. The first (Figure 7a) is a single phase scenario where fluid is injected in the vicinity of a transmissible fault that is initially mechanically stable. The second (Figure 7b) is a two-phase injection and production scenario in a faulted reservoir that is sealed above and below.

4.1 Model 1: Seismicity triggered by single-phase injection

The domain is illustrated in Figure 7a, and a set of physical parameters are applied as listed in Table 1. The injection well is operated at a constant bottom hole
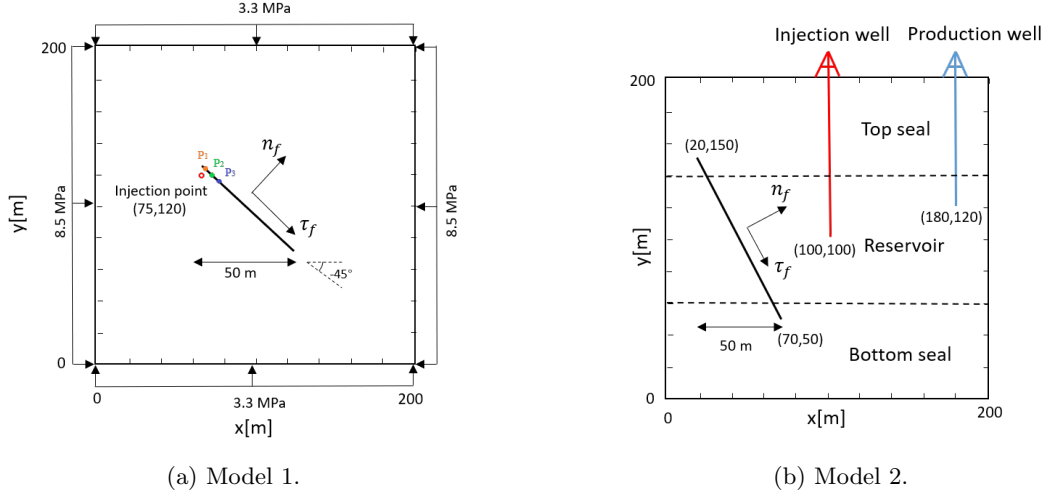
(a) Model 1.

(b) Model 2.

Figure 7: Two synthetic models a) a single phase injection scenario in the vicinity of a fault, and b) two phase injection and production in a faulted reservoir.

pressure of 5 MPa with reference to the uniform initial reservoir pressure of 0 MPa. The model is initialized under a diagonal far-field stress and this fixed initial pressure. That is, assuming that the fault is initially in a stable sticking condition under the static friction coefficient listed, the initial displacement field is obtained by enforcing static equilibrium. The simulation mesh is chosen such that the critical nucleation length ($L_c = 2.37$m in this case) is spanned by four elements. This provides sufficient resolution to capture rupture propagation fronts (Day et al., 2005). The investigation points P_1, P_2, and P_3 in Figure 7a are chosen at three consecutive locations along the fault, collocated with the expected elements that span L_c.

4.1.1 Simulated response

To illustrate the simulated evolution of the state variables, we apply the proposed hybrid time-step selection method using the linear CFF model and the time-stepping parameters listed in Table 2. The injection process is controlled by a fixed bottom-hole pressure. The resulting fluid injection rate into the completed matrix gridblock is a function of the difference between this fixed injection pressure and the pore pressure in the matrix rock. Specifically, we apply a linear well-index relationship (Aziz, 1979), and the computed injection rate is illustrated in Figure 8.

The fluid injection leads to a build-up in the pore pressure field that emanates outwards from the well, and towards the fault. Snapshots pf this evolution are presented in Figures 9(a)-(c). Moreover, the change in density of the compressible fluid evolves as presented by the snapshots in Figures 9(d)-(f).

These dynamics are also associated with a gradual reduction of the normal component of the effective traction on the fault, and the frictional strength according to Coulomb's law. While the fault is initially sticking, gradually, the frictional strength will become equal to and then exceed the external shear stress on the fracture. This triggers a slip instability as the difference between shear traction and frictional strength induces acceleration and drives a propagation of rupture. Upon reactivation, consecutive elements along the front experience slip consecutively. Once the length of the slipping elements reaches a critical value, nucleation is triggered. This occurs at a sim-

Table 1: Single phase injection case input parameters

Description	Value	Unit
Size	200×200	m$\times$m
Mesh	213×217	
matrix porosity ϕ_m	0.25	
matrix permeability K_m	1	mD
fracture porosity ϕ_f	1	
fracture initial aperture	0.11	mm
matrix Young's modulus E	40	GPa
matrix Poisson's ratio v	0.25	
matrix Biot's coefficient α	0.8	
fluid compressibility c_f	5.1×1^{-10}	1/Pa
fluid viscosity μ_f	1×10^{-3}	Pa·s
fluid reference density ρ_f	1000	kg/m^3
rock density ρ_s	3000	kg/m^3
reservoir initial pressure P_{ini}	0	MPa
injection pressure P_{inj}	5	MPa
static friction coefficient μ_s	0.6	
dynamic friction coefficient μ_d	0.4	
critical slip distance d_c	0.1	mm
P wave absorption coefficient a_p	1	
S wave absorption coefficient a_s	1	
Rayleigh damping coefficient a	2	
Rayleigh damping coefficient b	2.0×10^{-5}	
far-field stress tensor $\bar{t}$	[-8.5,0; 0,-3.3]	MPa

ulation time of approximately 120 hours. Figure 10 presents snapshots of the velocity field at various times after the onset of nucleation. Upon nucleation, the rupture front travels downwards along the fracture with accelerating rate until the leading rupture point arrives at the end of the fault. At this point, the induced seismic wave continues to propagate throughout the domain while the fracture slip velocity diminishes below the seismic slip threshold at which point, arrest occurs.

4.1.2 Comparison of time step control factors in capturing reactivation and transition to nucleation

The proposed hybrid controller simultaneously considers discretization error, CFF, and slip rate. To investigate the relative impacts of each of these considerations, we present simulation results using five alternative controllers. The combination of factors considered by each controller are presented in Table 3. Controller ATS1 naively applies a constant time step size of Δt_{max} until nucleation is observed, at which point slip rate control is applied thereafter. Table 3 also lists the times at which reactivation and nucleation are observed, as well as the number of time steps taken to reach these critical states. In all simulations, no time step cuts or repetitions were required, and the maximum number of nonlinear iterations required to converge time step solutions did not exceed five.

Figure 11 presents the series of time step sizes taken using each of the five control methods. In these figures, the markers indicate the limiting factor that led to the selection of the step size. Additionally, the predicted times for the onset of reactivation

Table 2: time-step controlling parameters

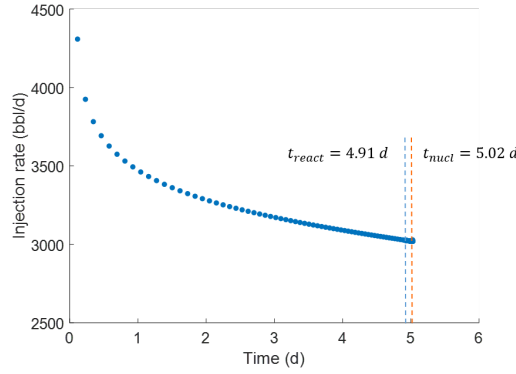| Parameter	Value	Units
Δt_{max}	10000	s
Δt_{min}	0.0002	s
ε_1	0.01	-
k_{min}	0.1	-
k_{max}	2	-
k_s	0.9	-
M	1	-
γ_{n+1}	0.3	-
γ_n	0.7	-
η	5e-6	-

Figure 8: Fluid injection rate due to a fixed injection bottom hole pressure.

and nucleation are indicated. As illustrated in Figure 11a, the ATS1 approach takes only three constant sized time steps between reactivation and nucleation. This implies that the predictions of quasi-static slip progression are particularly prone to discretization errors, and the time of onset of nucleation cannot be more precise than Δt_{max}. The ATS2 controller (Figure 11b) applies a slip rate consideration throughout, and prior to nucleation, it imposes step sizes that oscillate rapidly. Under sticking fracture conditions and at early times after reactivation, the slippage rate is nearly zero, and numerical errors lead to unreliable slip indicators. At later times past reactivation, these estimates are improved as the slippage rate is increased. ATS3 augments the slip rate consideration with discretization error control (Figure 12c). In this case, the discretization error is observed to be the only limiting factor prior to nucleation. Nevertheless, the time between reactivation and nucleation is once again poorly resolved. Finally, Figures 12 d and e present the results obtained using the proposed linear (ATS4) and quadratic (ATS5) methods. In both cases, the CFF criterion serves to ensure improved resolution during the interim period between reactivation and nucleation. During this period, both error and CFF considerations interplay to provide a refined definition of the time to nucleation. Implications of this capability are expected to also impact predictions of quasi-static slip that may not lead to nucleation. This is investigated further in a subsequent example.

Pore pressure

Density variation
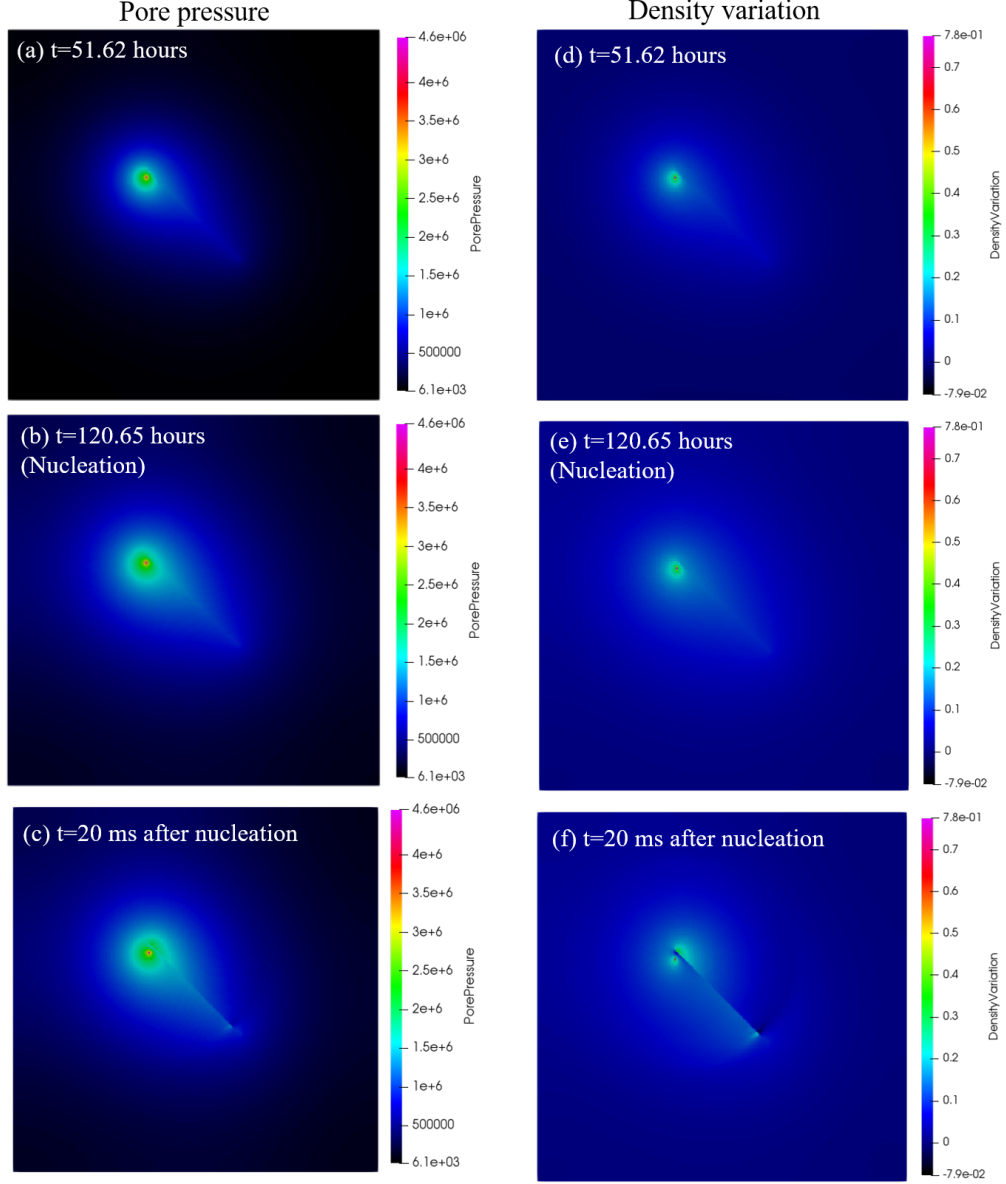
Figure 9: Snapshots of the pore pressure field (a)-(c) and density field (d)-(f) at various times: 51.62 hours, 120.65 hours (time of nucleation), and 20 ms after nucleation.
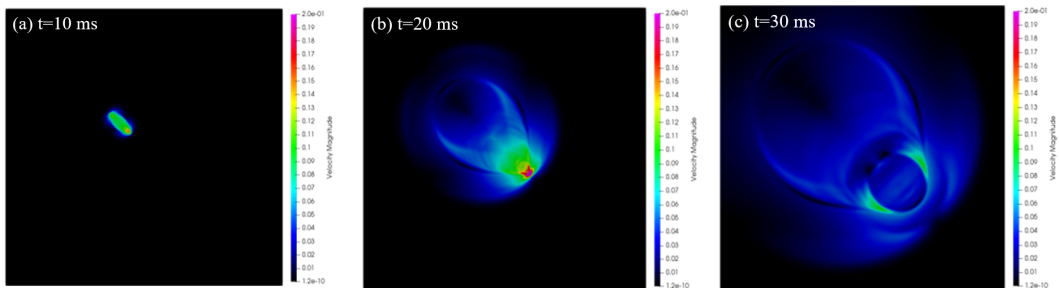

Figure 10: Snapshots of the magnitude of the particle velocity field at three selected times after the onset of nucleation: (a) t=10ms, (b) t=20ms, and (c) t=30ms
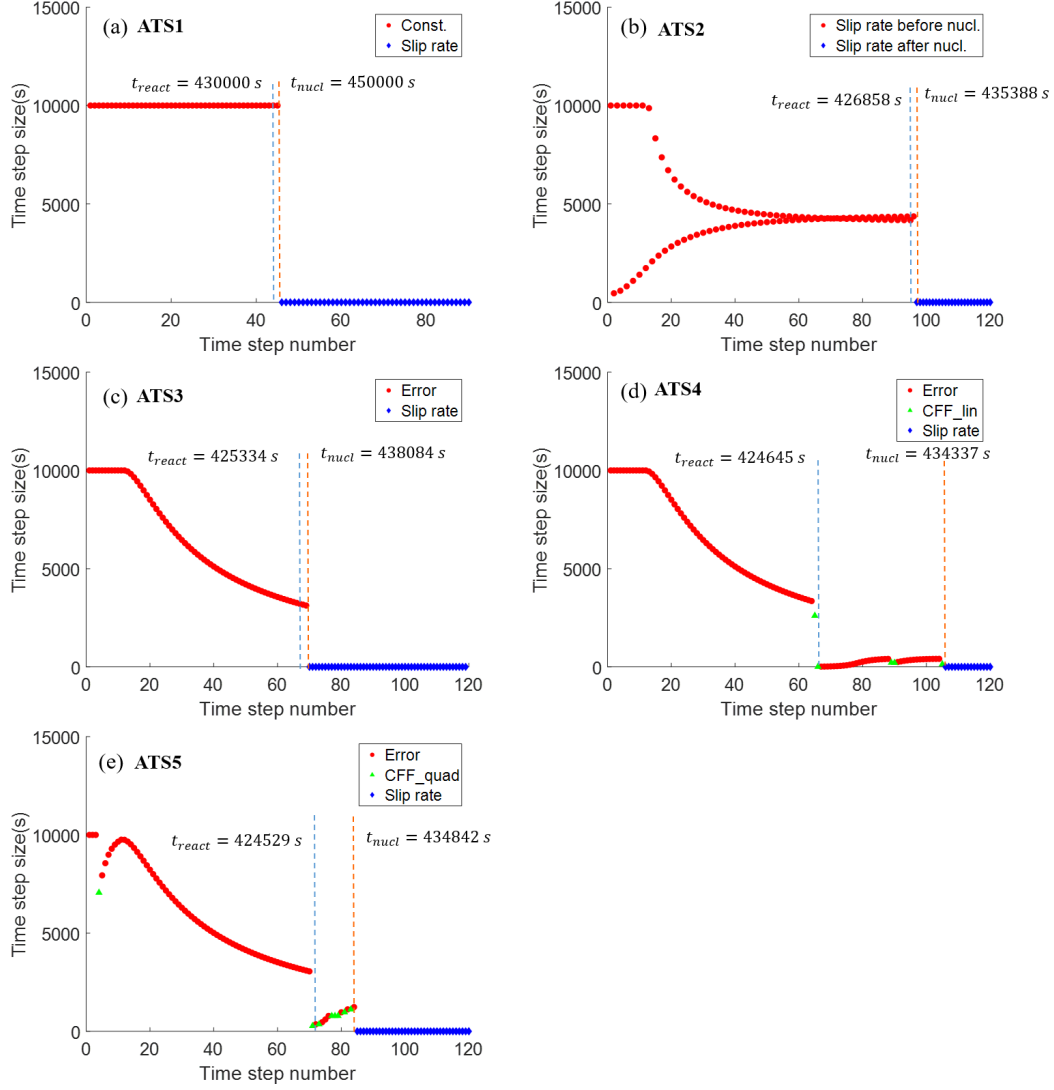
Figure 11: The series of time step sizes taken using 5 controllers: (a) ATS1, (b) ATS2, (c) ATS3, (d) ATS4, and (e) ATS5. Marker colors indicate the limiting selection factor.

Table 3: Five time step controllers used and the time to reactivation and nucleation, and number of time steps to nucleation and time step cuts.

| | Control factors | | | | | Performance metrics | | | |
	Const.	Slip rate	Error	CFF (lin.)	CFF (quad.)	React. [s]	Nucl. [s]	Steps to React.	Steps to Nucl.
ATS1	✓					430000	450000	44	46
ATS2		✓				426858	435388	94	96
ATS3		✓	✓			425334	438084	66	70
ATS4		✓	✓	✓		424645	434337	67	106
ATS5		✓	✓		✓	424529	434842	72	85

We further examine the relative efficacy of these methods in capturing the transitions across reactivation and nucleation. Figure 12 presents the time history of the computed estimates to the CFF function (Equation 41) evaluated at three consecutive elements along the fault (points P_1, P_2 and P_3 in Figure 7a). Using all five controllers, P_2 is the first location to experience slip (reactivation), followed by locations P_2 and P_3. Although this order is consistent for all methods, ATS4 and ATS5 appear to minimize the overshoot in CFF at the onset of reactivation. Figure 13a summarizes this finding using all methods for point P_2. Figure 13b presents the slipping patch locations on the fault at the time of onset of nucleation using all five methods. While all methods overestimate the theoretical critical sliding patch length, the ATS4 and ATS5 methods considerably outperform the other approaches with all other factors being equal.

4.1.3 Sensitivity to error tolerance

The ATS4 and ATS5 methods are utilized using two values of the discretization error tolerance, $\varepsilon_1 \in \{0.01, 0.1\}$. All other parameters remain unchanged. Figure 14 presents the simulation time step sizes taken using the two methods and the two tolerances. As expected, looser error tolerances lead to considerable differences in the predictions for the onset of reactivation. Nevertheless, the predictions for the onset of nucleation are relatively unchanged. This is also as expected since the CFF control criteria act to prevent time step size overshoot.

4.1.4 Sensitivity to the maximum allowable time-step size

In practice, the initial time step size is typically chosen to resolve the anticipated early dynamics; for example, the time for injected fluid to invade a single. Time step control seeks to adapt this scale as more simulation state information becomes available. In this test, we impose large initial time step sizes (injection to flood approximately 2500 cells in one time step), and we investigate controllers ATS4 and ATS5 to recover and capture reactivation and nucleation. With all other parameters of model 1 being equal, we present simulations using $\Delta t^0 = \Delta t_{max} \in \{50000s, 100000s\}$. Figure 15 presents the time step size series taken. In all cases, prior to reactivation, the error controller aggressively reduces the time step size. Additionally, the CFF criteria also contribute to step size reduction since the initial time step size is almost large enough to reach reactivation in one step. Despite the extreme starts, the controllers predict reactivation reasonably, and produce step sizes that are adequately refined to capture nucleation. While the overall number of time steps required for the simulations is reduced, the predictions for the onsets of rupture and nucleation vary considerably. Moreover, with larger time step sizes, we expect larger discretization error. This
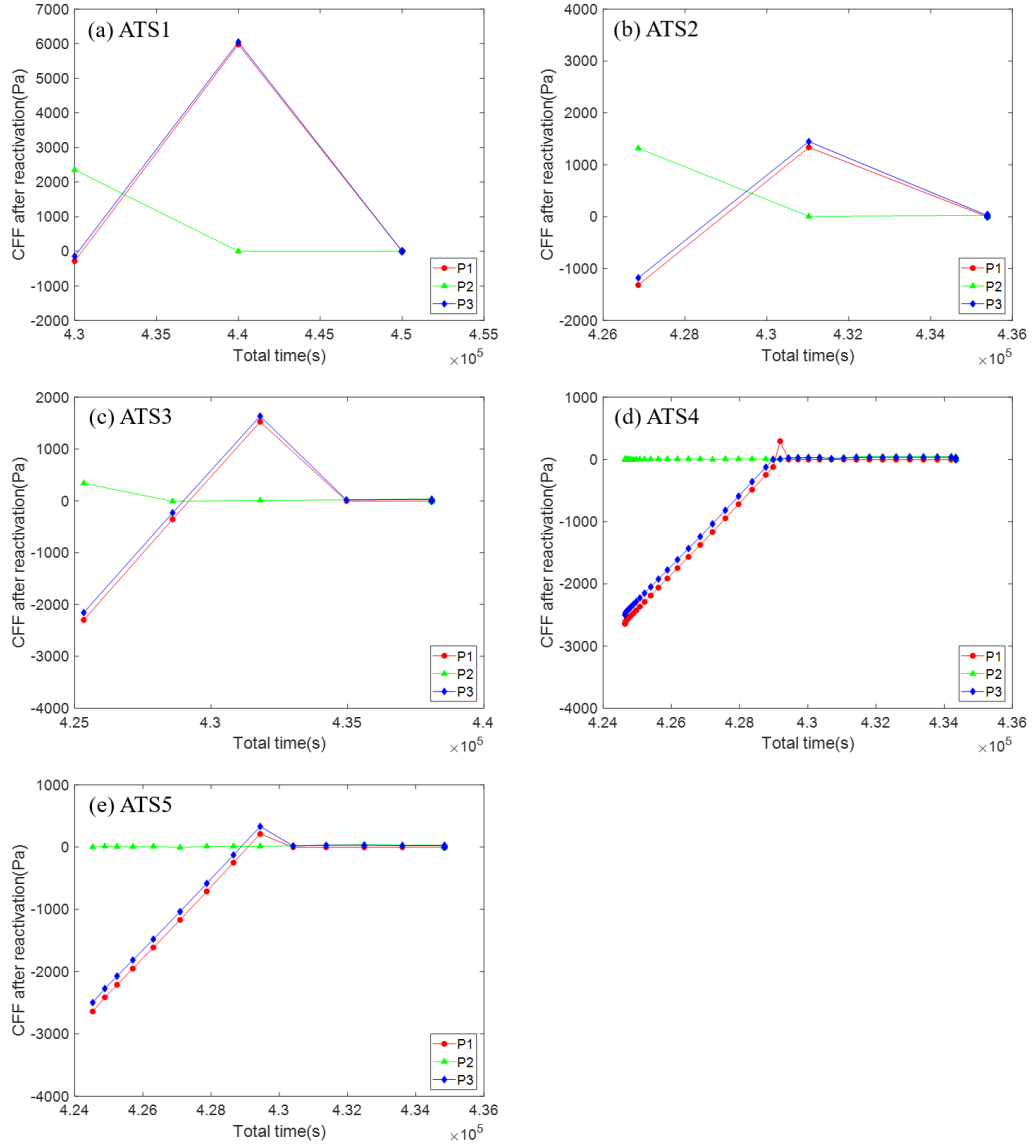
Figure 12: Summary of the results for CFF profile after fracture reactivation using 5 controllers: (a) ATS1, (b) ATS2, (c) ATS3, (d) ATS4, and (e) ATS5. Marker colors indicate three points selected along the fracture.
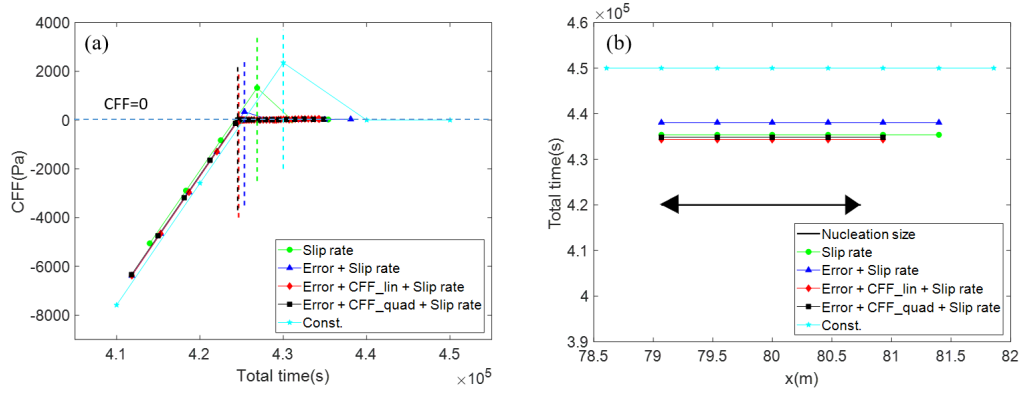
Figure 13: Analysis of reactivation and nucleation estimates: (a) Computed CFF evolution and predicted reactivation times at location P_2, and (b) Computed critical slipping patch lengths at nucleation.
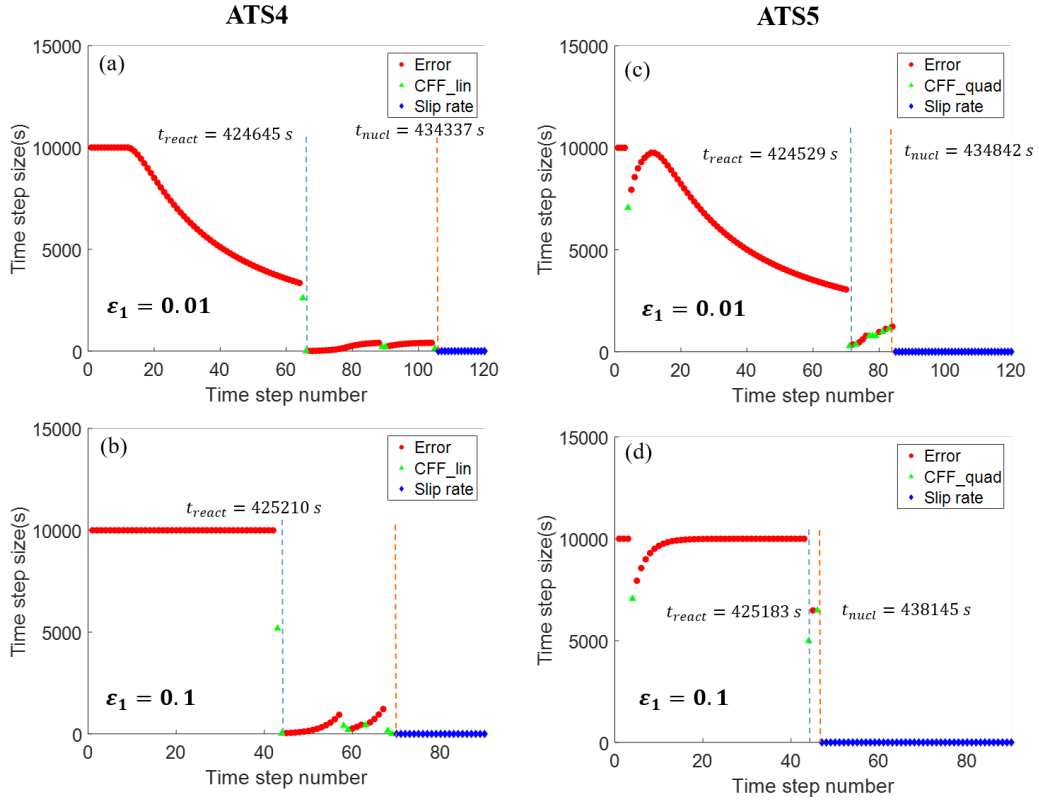

Figure 14: Simulation time step sizes taken using ATS4 and ATS5 with $\varepsilon_1 \in \{0.01, 0.1\}$.
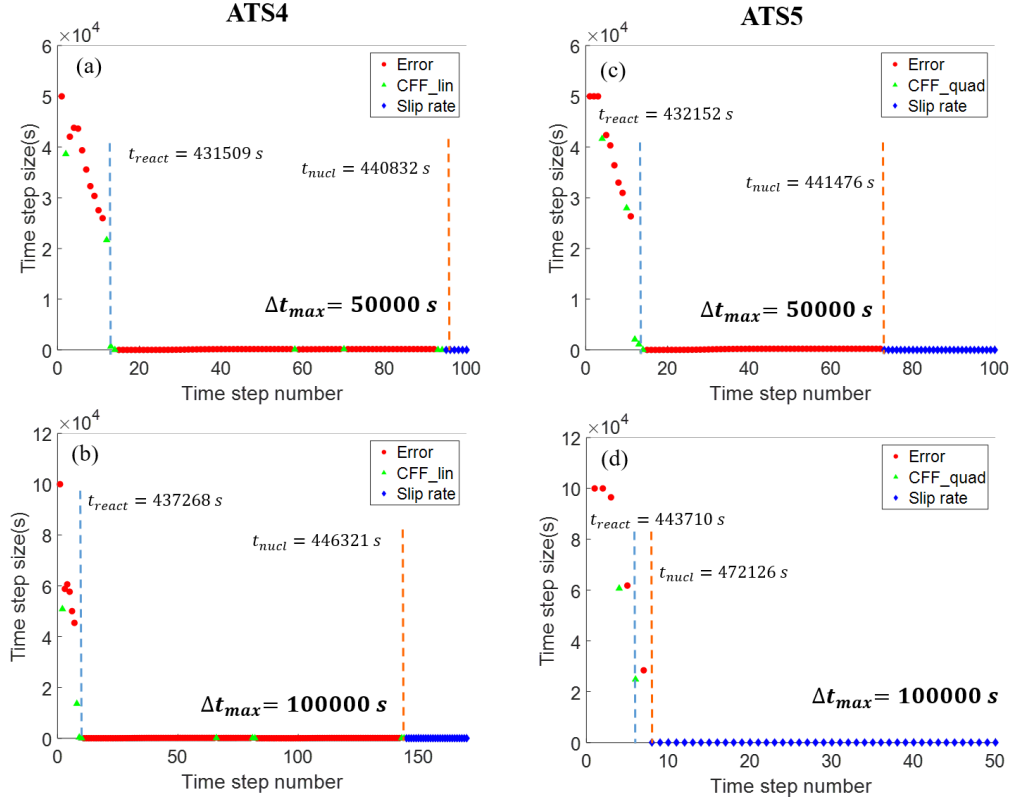
Figure 15: Time step series taken using ATS4 and ATS5 with $\varepsilon_1 = 0.01$: a) ATS4 and $\Delta t^0 = \Delta t_{max} = 50000s$; b) ATS4 and $\Delta t^0 = \Delta t_{max} = 100000s$; c) ATS5 and $\Delta t^0 = \Delta t_{max} = 50000s$; and d) ATS5 and $\Delta t^0 = \Delta t_{max} = 100000s$.
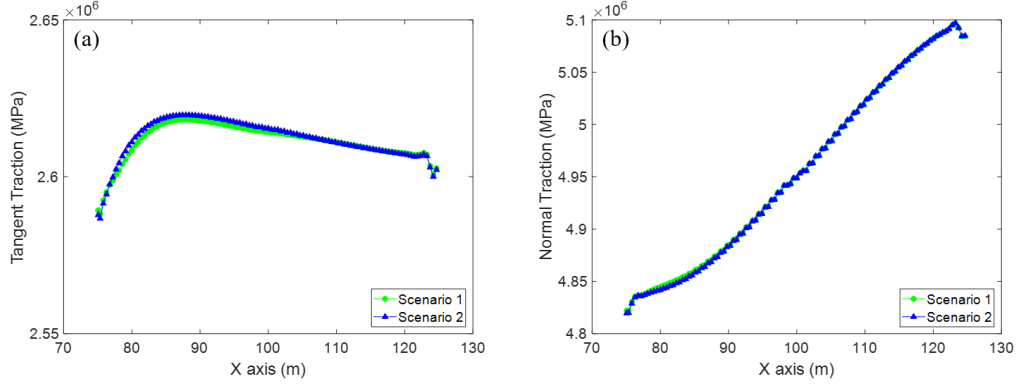
Figure 16: Traction profiles at equilibrium, following arrest using 5300 dynamic time steps (green) and a single quasi-static step (blue) after arrest: (a) tangential traction, (b) normal traction.

trade-off between computational expedience and accuracy can be leveraged to suit the purposes of simulation under different contexts.

4.1.5 Accuracy of the proposed treatment of arrest

In the proposed model, transitions from dynamic rupture (post-nucleation) to arrest are indicated by computed slip rates that drop below a threshold. These transitions are implemented by taking a single quasi-static time step upon arrest in order to equilibrate small scale transients in the field and allow the time step size to rapidly recover from a scale of milliseconds to days. Values for the threshold rate for dynamic slip v_{thresh} can range from 0.1 mm/s to 1 mm/s (McClure & Horne, 2011; McClure, 2015; Wynants-Morel et al., 2020). We select $v_{thresh} = 0.1$ mm/s and conduct simulations using ATS4 with a loose error tolerance of $\varepsilon_1 = 0.5$. Instead of applying a constant injection pressure at the well location, we apply a constant injection rate of 0.518 m^3/d and we stop the injection at the instant that nucleation occurs. In one simulation, we apply the proposed treatment for arrest (performing a single quasi-static solution step at arrest such that the fracture contact condition recovers to a sticking condition). In the other simulation, we continue with the minimum allowable time step size despite arrest, and subsequently resolve all small scale transients until they dissipate completely. Arrest is predicted to occur at 378789s by both models. Figure 16 presents the normal and tangential traction profiles at the final simulation time of $t = 378789s$ obtained using the two simulations. The maximum relative difference between the tangential and normal traction approximations are 0.1% and 0.06% respectively. Using dynamic time steps after arrest required over 5000 additional time steps to reach equilibrium, whereas the single quasi-static step approach accomplishes this in one step. This suggests that our proposed approach can be utilized to model multiple cycles of seismic events that are interspersed by periods of quasi-static behavior without a significant loss in accuracy and in an automated and computationally efficient manner.

4.1.6 Capturing multiple interspersed cycles of reactivation and nucleation.

We model two cycles of consecutively triggered seismic rupture. An injection rate of 0.518 m^3/d is imposed until the onset of the first nucleation. Injection is halted until seismic arrest, after which injection is resumed at a rate of 0.777 m^3/d until a second
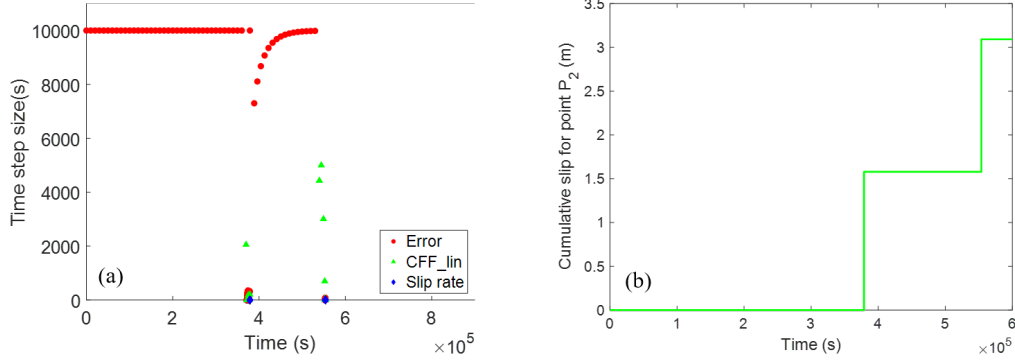
Figure 17: Two cycles of triggered seismic rupture: a) time step size series using ATS4, and b) the cumulative slippage at point P_2 over time.

nucleation event occurs. The time step size series and cumulative slippage for point P_2 obtained using ATS4 are presented in Figure 17. At the two nucleation events, the time step size is dramatically reduced to resolve the dynamics. Similarly, upon seismic arrest, the time step controller rapidly increases the time step size. This demonstrates effective automatic time step control across multiple transitions in the dynamics over timescales spanning seven orders of magnitude. Figure 18 presents the evolution of the slip and cumulative slip along the fracture during the first and second seismic rupture events. Rupture nucleates near the left end of the fracture and propagates along the fracture. The maximum slippage for the first and second events are 2.7mm and 2.4 mm respectively, and the cumulative slips are 2.4 m and 2.2 m respectively.

4.2 Model 2: Multi-phase injection and production operations

After evaluating the overall performance of the proposed methods for capturing the onset and arrest of rupture under single-phase fluid injection, we turn to the application of the proposed methodology to the simulation of earthquake sequences induced by two-phase fluid injection and production operations in a faulted reservoir (Figure 7b). Our objective is to demonstrate efficacy and capability. We defer the use of our model in illuminating scaling laws, motivating hypotheses pertaining to characteristic dynamics, and process engineering and design to future work.

In this model example, we study the impacts of injection rate and bottom hole production pressure on the nucleation and progression of seismic rupture. The simulation parameters used are listed in Table 4. Specifically, we consider two hypothetical well operation scenarios:

- Case 1: injection rate of $8.6 \times 10^{-5} \mathrm{m}^3/s$ (46.74 bbl/day) and a production-well bottom hole pressure of 0.5MPa (1 MPa below the initial reservoir pore pressure).
- Case 2: injection rate of $21.5 \times 10^{-5} \mathrm{m}^3/s$ (116.8 bbl/day) and a production-well bottom hole pressure of 1 MPa (0.5 MPa below the initial reservoir pore pressure).

For these parameters, the critical slipping patch length for nucleation is $L_c =3.45$m, and five simulation mesh elements are used to span this length.
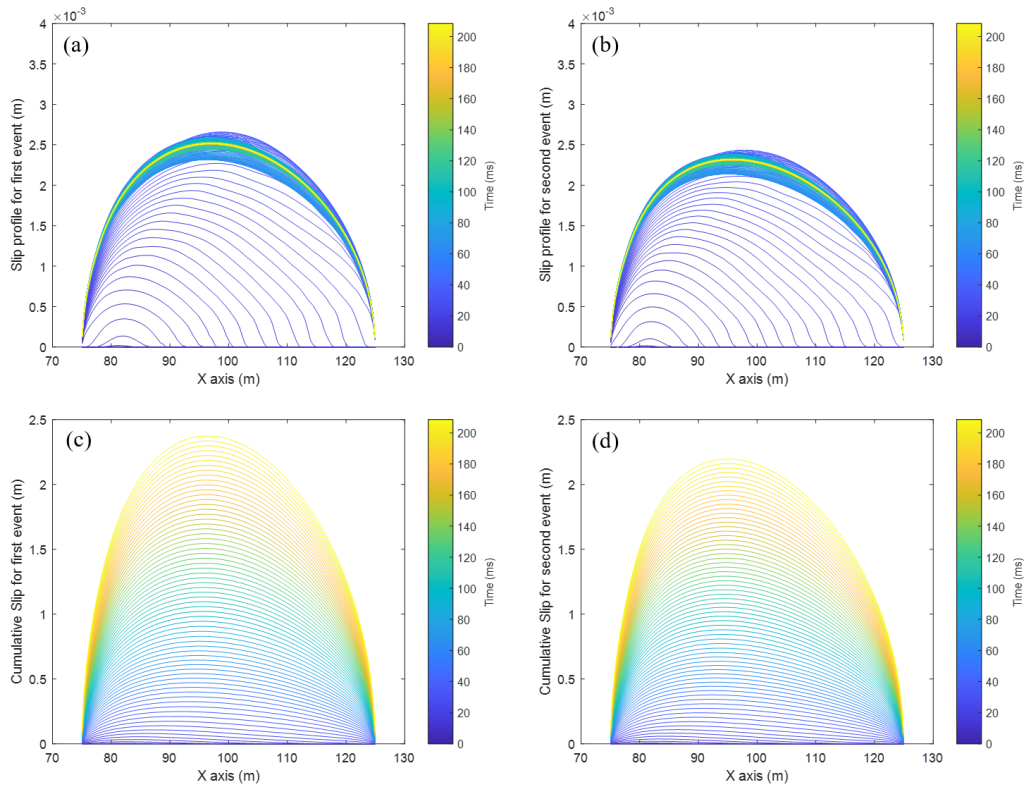
Figure 18: Slip profile and cumulative slip profile for first (a-b) and second seismic events (c-d)

Table 4: Model 2 simulation case input parameters

| Description	Value	Unit
Size	200×200	m×m
Mesh	213×217	
reservoir porosity ϕ_r	0.25	
reservoir permeability K_r	1	mD
seal porosity ϕ_s	0.1	
seal permeability K_s	1	μD
fracture porosity ϕ_f	1	
fracture initial aperture	0.11	mm
matrix Young's modulus E	40	GPa
matrix Poisson's ratio v	0.4	
matrix Biot's coefficient α	0.8	
water compressibility c_w	5.1×10^{-10}	1/Pa
oil compressibility c_o	3.5×10^{-9}	1/Pa
water viscosity μ_w	5×10^{-4}	Pa·s
oil viscosity μ_o	1×10^{-4}	Pa·s
water reference density ρ_w	897	kg/m^3
oil reference density ρ_o	800	kg/m^3
rock density ρ_s	3000	kg/m^3
residual oil saturation S_{or}	0.05	
residual water saturation S_{wr}	0.15	
water relative perm end point K_{rw}^{end}	1.0	
oil relative perm end point K_{ro}^{end}	1.0	
water exponential term N_w	2.5	
oil exponential term N_o	2.5	
reservoir initial pressure P_{ini}	1.5	MPa
static friction coefficient μ_s	0.6	
dynamic friction coefficient μ_d	0.4	
critical slip distance d_c	0.12	mm
P wave absorption coefficient a_p	1	
S wave absorption coefficient a_s	1	
Rayleigh damping coefficient a	6	
Rayleigh damping coefficient b	6.0×10^{-5}	
far-field stress tensor $\bar{t}$	[-8.5,0; 0,-3.3]	MPa
Case 1 injection rate	8.6×10^{-5}	m$^3/s$
Case 1 production pressure	0.5	MPa
Case 2 injection rate	2.15×10^{-4}	m$^3/s$
Case 2 production pressure	1	MPa
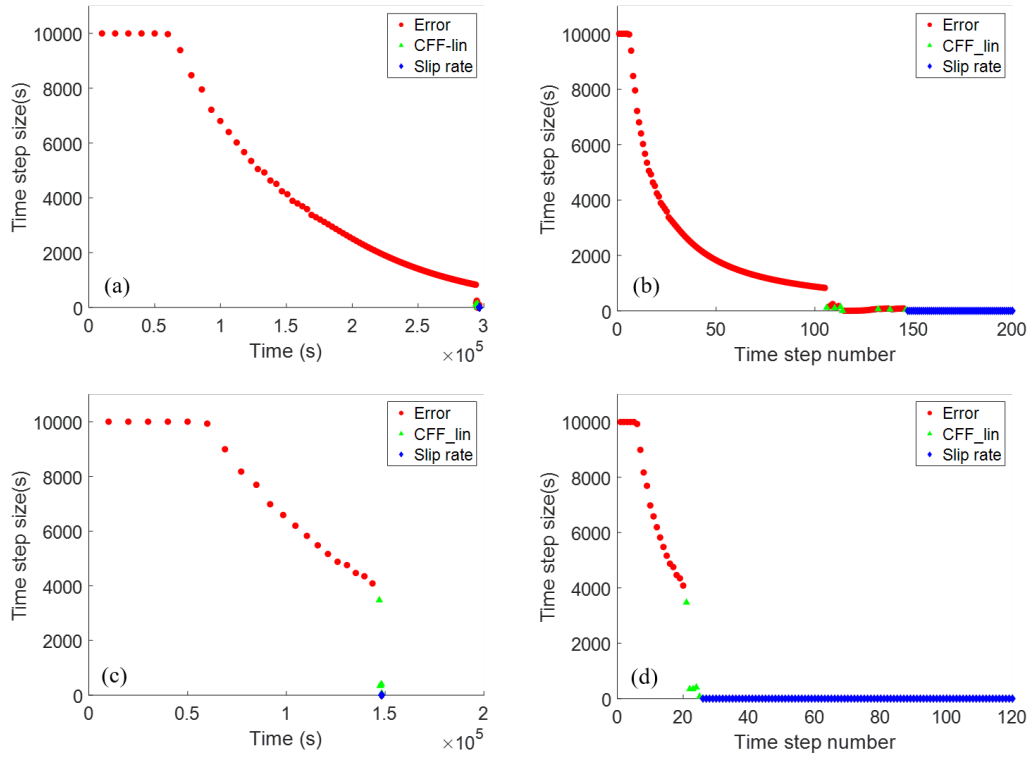
Figure 19: Summary of the time step size series obtained for two well operation scenarios: (a-b) case 1, (c-d) case 2
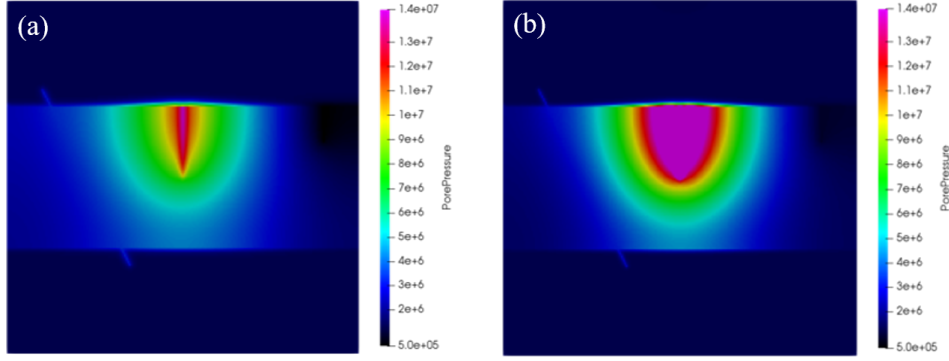
Figure 20: Snapshots of the pressure field at nucleation time: (a) case 1: pressure field at 3.43 days, (b) case 2: pressure field at 1.72 days
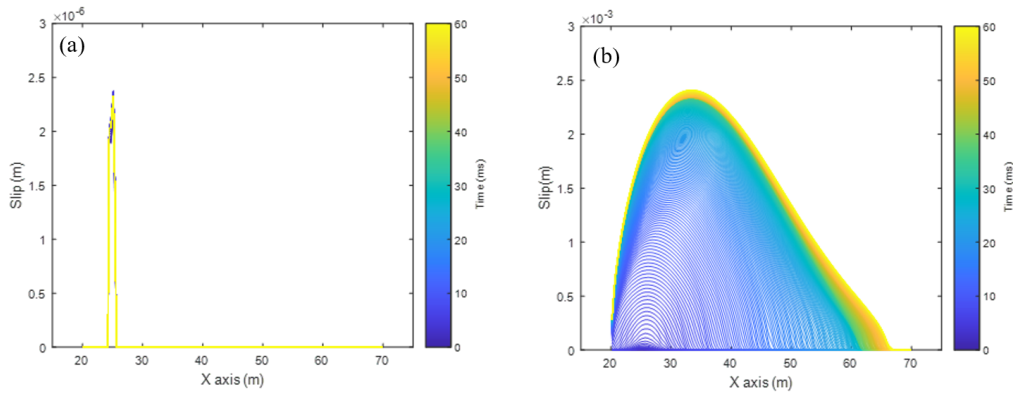

Figure 21: Slip profiles along the fault plotted every 0.2 ms over a duration of 60 ms:(a) case 1, (b) case 2

Figure 19 presents the evolution of the time step size for both cases using the ATS4 time step controller. The onset of nucleation for case 1 occurs after 3.43 days whereas that for case 2 occurs sooner at 1.72 days. Upon nucleation, a time step size of 0.2 ms is used in both cases. Figure 20 presents the pore pressure fields for cases 1 and 2 at their respective onsets of nucleation. Case 2 exhibits a higher pore pressure in the vicinity of the injection well due despite the lower production pressure. Figure 21 presents the slip evolution along the fracture during dynamic rupture. For case 1, only fracture locations within the vicinity of the nucleation patch exhibit slippage, and with a maximum value of approximately 2.4×10^{-6} m. In case 2 on the other hand, seismic rupture propagates along the entire length of the fracture. The slip profile for case 2 shows that the rupture nucleates near the left end of the fracture. The rupture front moves towards the other end and gradually expands along the fracture. The slippage for each time step increases with time and the maximum magnitude of slip is around 2.4×10^{-3} m which is much larger than that for case 1.

Finally, Figure 22 presents snapshots the velocity fields for both cases at two times after nucleation. For case 1, a wave propagates outwards from the nucleation region which acts almost as a point source. Furthermore the magnitude of propagation velocity dissipates over time from approximately 1×10^{-4} m/s to 6×10^{-6}, which is below the seismic rupture velocity threshold range. For case 2, the rupture front develops and becomes increasingly visible. The peak magnitude of velocity is greater

than 0.01 m/s. After the rupture front reaches the end of the fracture, a seismic wave propagates through the domain as the slip velocity along the fracture decays.
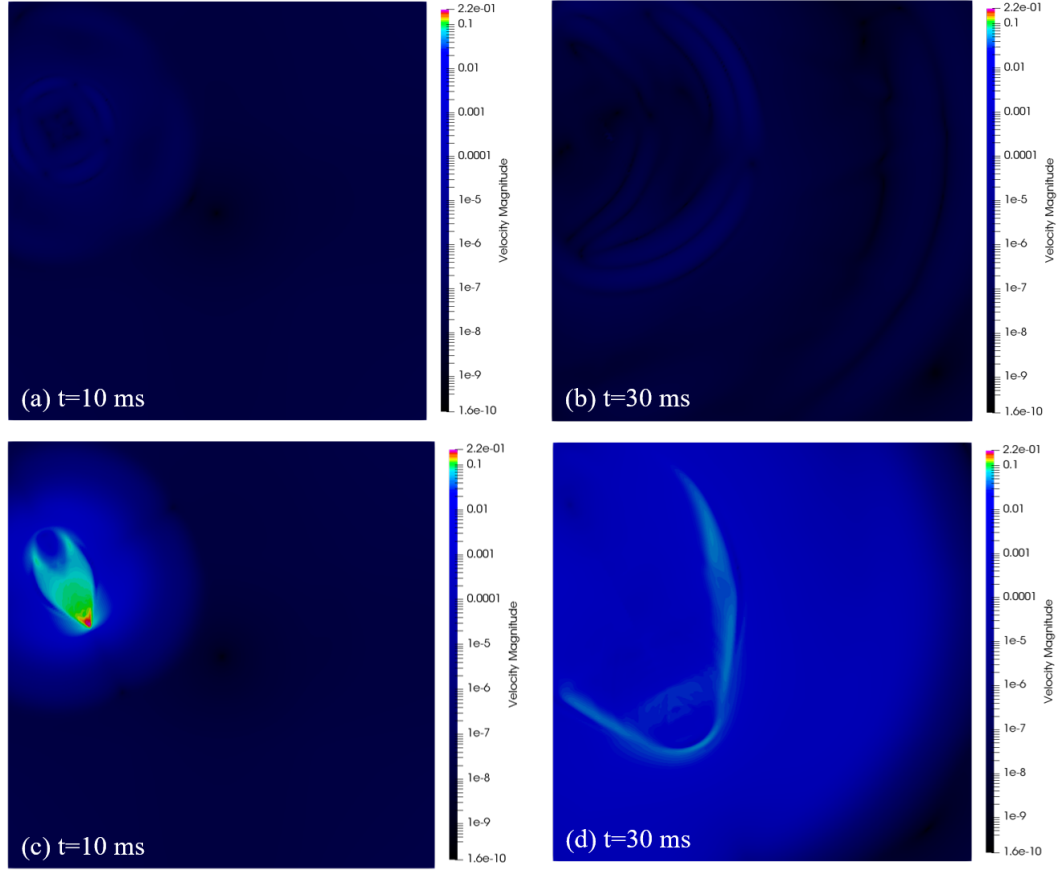

Figure 22: Snapshots of the spatial distribution of the magnitude of the particle velocity after nucleation:(a-b) case 1 at t=10ms and t=30ms after nucleation, (c-d) case 2 at t=10ms and t=30ms after nucleation

5 Discussion and Conclusions

A seamless and time-adaptive numerical model is proposed for the simulation of multiphase flow and deformation in fractured formations. The model approximates transient poromechanics and multiphase flow in fractured reservoirs using a hybrid XFEM and pEDFM approach. The temporal discretization of mechanical inertia is accomplished using an implicit and unconditionally stable Newmark scheme. Fracture contact constraints are enforced using a Lagrange Multiplier method that captures stick-slip behavior. Computational examples apply a slip-weakening frictional model. We develop a novel time-step controller to capture the onset of fracture rupture and nucleation, should they occur. The controller is designed to automatically scale the simulation time-step size over seven orders of magnitude as necessary. The controller combines discretization error, Coulomb failure, and slip rate considerations to automatically adjust time-stepping to resolve the interseismic period and dynamic rupture within the allowed accuracy. The seamless model could be used in scenarios where no seismicity is to occur without any significant loss in computational efficiency. On the other hand, should quasi-static slip occur, the model will resolve this behavior at a

592   suitable temporal resolution. Finally, under dynamic rupture, the model not only cap-
593   tures the fast dynamics, but is also capable of recovering automatically to drastically
594   larger time scales upon arrest.

595   In addition to computer implementations of the proposed model in three di-
596   mensions, a number of refinements may be the subject of future work. The three
597   time scales considered (multiphase flow with small deformation, quasi-static fracture
598   slip, and dynamic rupture and wave propagation) are associated with widely different
599   spatial supports for the changes in the solution state. More specifically, during dy-
600   namic rupture, the fluid state fields exhibit changes that are localized to the vicinity
601   of traveling mechanical waves. This behavior can be exploited by adaptive solution
602   (e.g. R. Younis et al. (2010); S. M. Sheth and Younis (2017); S. Sheth et al. (2021))
603   or mesh refinement methods. In terms of applications, the proposed seamless model
604   may be used in a CLRM context to simultaneously assimilate flow, microseismic, and
605   seismic data in a single model without a need for methods to cross-inform stitched
606   components. Additionally, the model may enable the study of causal relationships the
607   cross the three physical regimes considered.

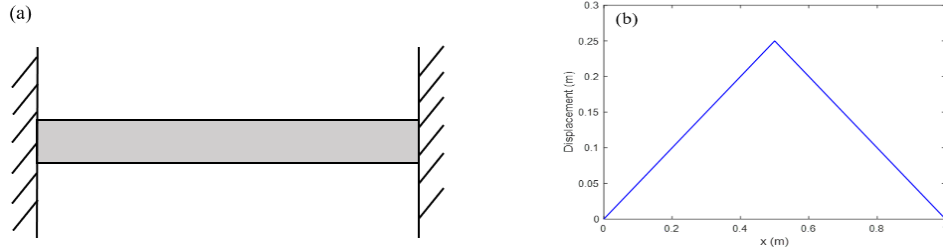## Appendix A   Validation of temporal discretization

608

Figure A1: An elastic bar that is fixed at two ends and subjected to an initial displace-
ment field: (a) schematic of the model problem, (b) initial displacement field

609   The implementation is applied to simulate a benchmark model problem presented
610   in Torii and Machado (2012). The model problem is that of an elastic bar (non-
611   porous) of length $1m$ that is fixed at both ends (FigureA1a). The mid-point of the
612   bar is initially stretched towards the fixed right end (FigureA1b), and at $t = 0$ is
613   released. With no dissipation, the displacement field will oscillate indefinitely due to
614   the elasticity of the material and the fixed ends. The material elasticity and density
615   are set as $E = 1$ Pa and $\rho = 1$ kg/m^3 such that the characteristic wave speed
616   is $c = \sqrt{E/\rho} = 1m/s$. An analytical solution is readily obtained by separation of
617   variables. We compare numerical estimates obtained with our implementation using
618     $\delta = 0.5$ and $\beta = 0.25$ to the analytical solution. Note that the fluid flow equations and
619   fracture models are absent in this case. To illustrate the solution response, Figure A2
620   shows results obtained over a time interval of 10s. The numerical solution is obtained
621   using a mesh size of 10000 elements and a fixed $\Delta t = 0.001s$. The analytical and
622   numerical solutions are in agreement: Figure A2a shows a snapshot of the displacement
623   field at $t = 1s$, and Figure A2b shows the time evolution of the displacement of the
624   mid-point of the bar.

We conduct an asymptotic mesh refinement study following the approaches of (Jameson
& Martinelli, 1998). We consider two alternate meshes comprised of 100 and 10000 ele-
ments, and a set of alternate constant time step sizes; $\Delta t \in \{0.1s, 0.01s, 0.001s, 0.0001s\}$.
Note that the time step sizes to attain a Courant–Friedrichs–Lewy (CFL) number of
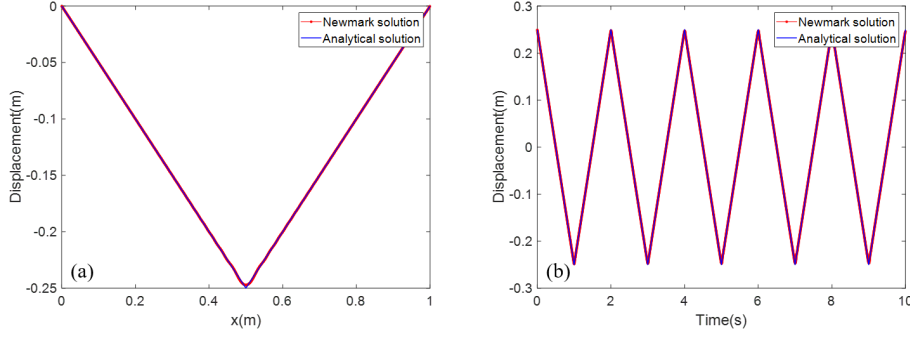
Figure A2: Simulated (red) and analytical (blue) response: (a) displacement fields at $t = 1s$, and (b) displacement evolution of the mid-point,
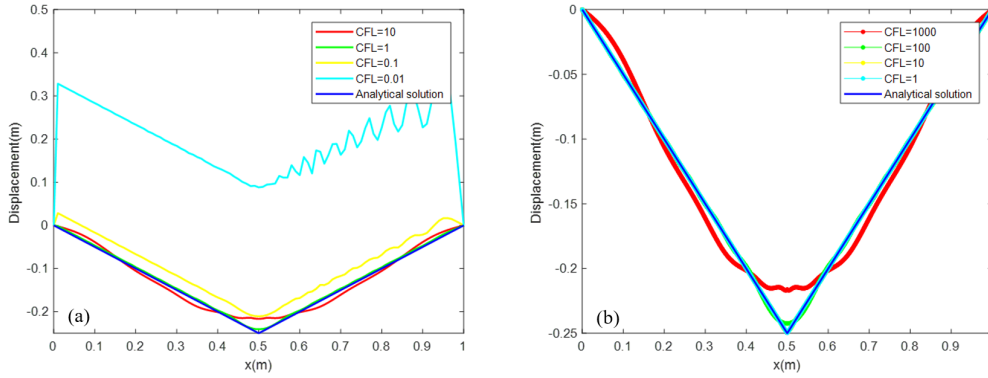

Figure A3: Displacement field snapshots at $t = 1s$ obtained using various constant time step sizes and two meshes: (a) mesh size 100 and (b) mesh size 10000.

one for the two meshes are $0.01s$ and $0.0001s$ respectively. Additionally, the computed error for a given simulation mesh Ω_h and time t^n is defined as,

$$\epsilon_h^n := \mathbf{u}_h^n - \mathbf{u}\left(\Omega_h, t^n\right).$$

Figure A3 shows snapshots of the displacement field at $t = 1s$ obtained using time step sizes ranging from $0.1s$ to $0.0001s$. For the coarse mesh, these correspond to CFL numbers ranging from 10 to 0.01, and for the fine mesh, they range from 1000 to 1. As expected, with CFL numbers greater than one, the numerical solutions approach the analytical solution. With CFL numbers less than one, oscillatory (dispersive) error modes dominate, and become more prevalent with reduced CFL number. This behavior is well-studied in Hughes (2012), and for the purposes of our implicit approach, this is not an issue; the proposed method is aimed at simulation with CFL numbers greater than 1. Figure A4 provides a quantitative view of the asymptotic accuracy. At CFL numbers greater than one, the asymptotic accuracy in both the one- and infinity-norms is at least first-order accurate. At CFL numbers below one, the oscillatory modes will dominate.
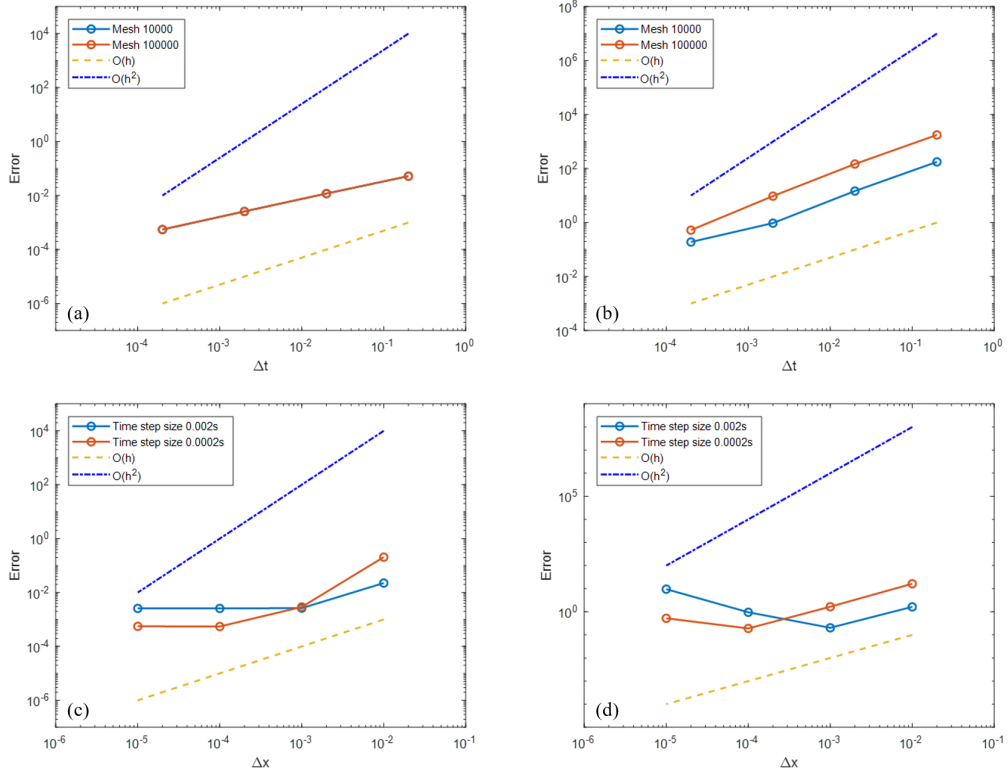
Figure A4: Asymptotic error profiles : (a) $\|\epsilon_h^n\|_\infty$ with time refinement, (b) $\|\epsilon_h^n\|_1$ with time refinement, (c) $\|\epsilon_h^n\|_\infty$ with spatial refinement, and (d) $\|\epsilon_h^n\|_1$ with spatial refinement.
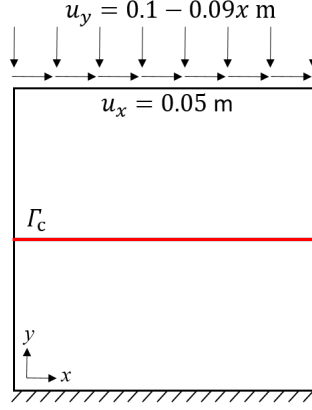
Figure B1: A straight interface under nonuniform compression; Geometry and boundary conditions

Appendix B Validation of contact fracture sticking and slipping conditions

This case is studied to evaluate the performance of Lagrange Multiplier method considering the behavior of the stick and slip condition under non-uniform compression, as shown in Khoei (2014). The domain is $[0,1] \times [0,1]$ with the fracture intersected in the middle, as shown in Figure B1. The top boundary has prescribed displacement both in the x and y directions, and the displacement of the y direction changes along the boundary that causes the stick-slip behavior. The bottom boundary is constrained both in the vertical and horizontal directions. The simulations with two friction coefficients $\mu = 0.1$ and $\mu = 0.4$ are implemented under the mesh of 75×75. [h] For
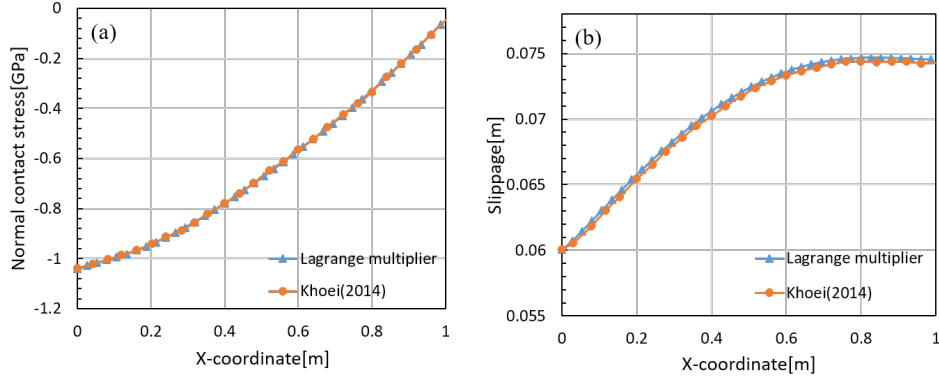

Figure B2: Straight interface under nonuniform compression with $\mu = 0.1$: (a) profile of normal stress along the contact interface, (b) profile of slippage along the contact interface

the coefficient $\mu = 0.1$, the contact interface is under the slip condition, the profiles of normal stress and slippage are plotted in Figure B2. Owing to the nonuniform displacement in y direction on the top boundary, the normal stress varies along the fracture and the place with smaller boundary displacement results in smaller normal contact traction, correspondingly, it has a larger slippage. For the coefficient $\mu = 0.4$,
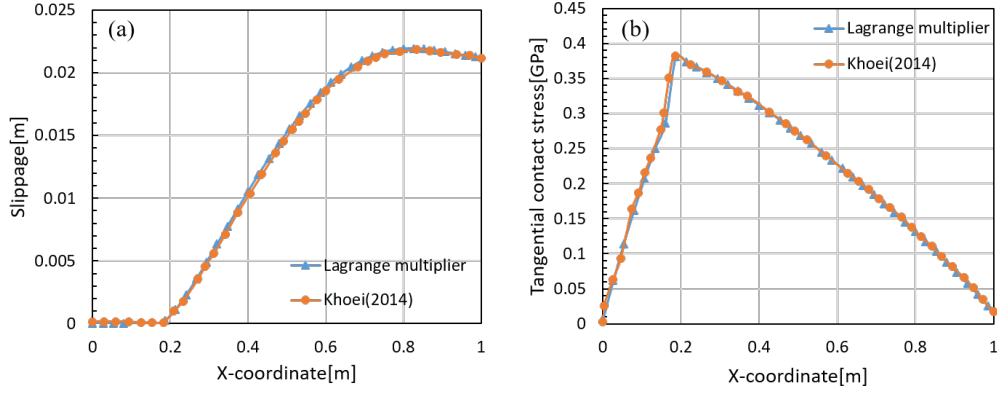
Figure B3: Straight interface under nonuniform compression with $\mu = 0.4$: (a) profile of slippage along the contact interface (b) profile of tangential stress along the contact interface

the normal contact stress is identical to the former case because the normal traction is independent of the stick and slip condition. However, for the slippage and tangential stress, the interface has two regions with the stick and slip behaviors, as shown in Figure B3. In the stick region, the relative movement is zero and the tangential stress is below the static friction force, and it gradually increases to the critical value along the fracture. In the slip region, the tangential traction is determined using the static friction model and the slippage is allowed on the interface.

Acknowledgments

References

Aagaard, B. T., Knepley, M. G., & Williams, C. A. (2013, jun). A domain decomposition approach to implementing fault slip in finite-element models of quasi-static and dynamic crustal deformation. *Journal of Geophysical Research: Solid Earth*, *118*(6), 3059–3079. doi: 10.1002/JGRB.50217

Andrews, D. J. (1976). Rupture velocity of plane strain shear cracks. *Journal of Geophysical Research*, *81*(32), 5679–5687.

Aziz, K. (1979). Petroleum reservoir simulation. *Applied Science Publishers*, *476*.

Biot, M. A. (1941). General theory of three-dimensional consolidation. *Journal of applied physics*, *12*(2), 155–164.

Buijze, L., Van Den Bogert, P. A., Wassing, B. B., Orlic, B., & Ten Veen, J. (2017). Fault reactivation mechanisms and dynamic rupture modelling of depletion-induced seismic events in a rotliegend gas reservoir. *Netherlands Journal of Geosciences*, *96*(5), s131–s148.

Buijze, L., van den Bogert, P. A. J., Wassing, B. B. T., & Orlic, B. (2019). Nucleation and arrest of dynamic rupture induced by reservoir depletion. *Journal of Geophysical Research: Solid Earth*, *124*(4), 3620–3645.

Cao, H. (2002). *Development of techniques for general purpose simulators*. Stanford University.

Cappa, F., & Rutqvist, J. (2011, mar). Modeling of coupled deformation and permeability evolution during fault reactivation induced by deep underground injection of CO2. *International Journal of Greenhouse Gas Control*, *5*(2), 336–346. doi: 10.1016/J.IJGGC.2010.08.005

Cappa, F., & Rutqvist, J. (2012, sep). Seismic rupture and ground accelerations induced by CO 2 injection in the shallow crust. *Geophysical Journal International*, *190*(3), 1784–1789. doi: 10.1111/J.1365-246X.2012.05606.X

Cueto-Felgueroso, L., Santillán, D., & Mosquera, J. C. (2017). Stick-slip dynamics of flow-induced seismicity on rate and state faults. *Geophysical Research Letters*, *44*(9), 4098–4106.

Cueto-Felgueroso, L., Vila, C., Santillán, D., & Mosquera, J. C. (2018, dec). Numerical Modeling of Injection-Induced Earthquakes Using Laboratory-Derived Friction Laws. *Water Resources Research*, *54*(12), 9833–9859. doi: 10.1029/2017WR022363

Curnier, A. (1984). A theory of friction. *Int. J. Solids Struct.*, *20*, 637–647.

Day, S. M., Dalguer, L. A., Lapusta, N., & Liu, Y. (2005). Comparison of finite difference and boundary integral solutions to three-dimensional spontaneous rupture. *Journal of Geophysical Research: Solid Earth*, *110*(B12).

Dean, R. H., Gai, X., Stone, C. M., & Minkoff, S. E. (2006). A comparison of techniques for coupling porous flow and geomechanics. *SPE Journal*, *11*(01), 132–140.

Géradin, M., & Rixen, D. J. (2014). *Mechanical vibrations: theory and application to structural dynamics*. John Wiley & Sons.

Han, Z., Ren, G., & Younis, R. (2020). Coupled forward simulation of seismicity: A stick-slip model for fractures and transient geomechanics. *ECMOR 2020 - 17th European Conference on the Mathematics of Oil Recovery*.

Hughes, T. J. R. (2012). *The finite element method: linear static and dynamic finite element analysis*. Courier Corporation.

Jameson, A., & Martinelli, L. (1998). Mesh refinement and modeling errors in flow simulation. *AIAA journal*, *36*(5), 676–686.

Jansen, J. D., Bosgra, O. H., & Van den Hof, P. M. (2008, oct). Model-based control of multiphase flow in subsurface oil reservoirs. *Journal of Process Control*, *18*(9), 846–855. doi: 10.1016/J.JPROCONT.2008.06.011

Jansen, J.-D., Brouwer, D., Naevdal, G., & van Kruijsdijk, C. P. J. W. (2005, jan). Closed-loop reservoir management. *First Break*, *23*(1), 856–873. doi: 10.3997/1365-2397.2005002

Jha, B., & Juanes, R. (2014). Coupled multiphase flow and poromechanics: A computational model of pore pressure effects on fault slip and earthquake triggering. *Water Resources Research*, *50*(5), 3776–3808.

Jiang, J., & Younis, R. M. (2015a). A multimechanistic multicontinuum model for simulating shale gas reservoir with complex fractured system. *Fuel*, *161*, 333–344.

Jiang, J., & Younis, R. M. (2015b). Numerical study of complex fracture geometries for unconventional gas reservoirs using a discrete fracture-matrix model. *Journal of Natural Gas Science and Engineering*, *26*, 1174–1186.

Jiang, J., & Younis, R. M. (2016a). Compositional modeling of enhanced hydrocarbons recovery for fractured shale gas-condensate reservoirs with the effects of capillary pressure and multicomponent mechanisms. *Journal of Natural Gas Science and Engineering*, *34*, 1262–1275.

Jiang, J., & Younis, R. M. (2016b, jun). Hybrid coupled discrete-fracture/matrix and multicontinuum models for unconventional-reservoir simulation. *SPE Journal*, *21*(3), 1009–1027. doi: 10.2118/178430-PA

Jiang, J., & Younis, R. M. (2017). An improved projection-based embedded discrete fracture model (pEDFM) for multiphase flow in fractured reservoirs. *Advances in Water Resources*, *109*, 267–289. doi: 10.1016/j.advwatres.2017.09.017

Jin, L., & Zoback, M. D. (2018, nov). Fully dynamic spontaneous rupture due to quasi-static pore pressure and Poroelastic effects: An implicit nonlinear computational model of fluid-induced seismic events. *Journal of Geophysical Research: Solid Earth*, *123*(11), 9430–9468. doi: 10.1029/2018JB015669

Khoei, A. R. (2014). *Extended finite element method: theory and applications.* John Wiley & Sons.

Khoei, A. R., & Nikbakht, M. (2007). An enriched finite element algorithm for numerical computation of contact friction problems. *International Journal of Mechanical Sciences*, *49*(2), 183–199.

Lee, S. H., Lough, M. F., & Jensen, C. L. (2001, mar). Hierarchical modeling of flow in naturally fractured formations with multiple length scales. *Water Resources Research*, *37*(3), 443–455. doi: 10.1029/2000wr900340

Li, L., & Lee, S. H. (2008, aug). Efficient Field-Scale Simulation of Black Oil in a Naturally Fractured Reservoir Through Discrete Fracture Networks and Homogenized Media. *SPE Reservoir Evaluation & Engineering*, *11*(04). doi: 10.2118/103901-PA

Liu, F., & Borja, R. I. (2010). Stabilized low-order finite elements for frictional contact with the extended finite element method. *Computer Methods in Applied Mechanics and Engineering*, *199*(37-40), 2456–2471.

Liu, M., & Gorman, D. G. (1995). Formulation of Rayleigh damping and its extensions. *Computers & structures*, *57*(2), 277–285.

Lysmer, J., & Kuhlemeyer, R. L. (1969). Finite dynamic model for infinite media. *Journal of the Engineering Mechanics Division*, *95*(4), 859–878.

Mathews, J. H., & Fink, K. D. (2004). *Numerical methods using matlab* (Vol. 4). Pearson prentice hall Upper Saddle River, NJ.

Mayr, M., Wall, W. A., & Gee, M. W. (2018). Adaptive time stepping for fluid-structure interaction solvers. *Finite Elements in Analysis and Design*, *141*, 55–69.

McClure, M. W. (2015). Generation of large postinjection-induced seismic events by backflow from dead-end faults and fractures. *Geophysical Research Letters*, *42*(16), 6647–6654.

McClure, M. W., & Horne, R. N. (2011). Investigation of injection-induced seismicity using a coupled fluid flow and rate/state friction model. *Geophysics*, *76*(6), WC181—-WC198.

Meng, C. (2017). Benchmarking Defmod, an open source FEM code for modeling episodic fault rupture. *Computers & Geosciences*, *100*, 10–26.

Meng, C., & Wang, H. (2018). A finite element and finite difference mixed approach for modeling fault rupture and ground motion. *Computers & Geosciences*, *113*, 54–69.

Moës, N., Dolbow, J., & Belytschko, T. (1999). A finite element method for crack growth without remeshing. *International journal for numerical methods in engineering*, *46*(1), 131–150.

Moinfar, A., Varavei, A., Sepehrnoori, K., & Johns, R. T. (2013, jul). Development of an Efficient Embedded Discrete Fracture Model for 3D Compositional Reservoir Simulation in Fractured Reservoirs. *SPE Journal*, *19*(02), 289–303. doi: 10.2118/154246-PA

Newmark, N. M. (1959). A method of computation for structural dynamics. *Journal of the engineering mechanics division*, *85*(3), 67–94.

Paap, B., Kraaijpoel, D., Wassing, B., & Van Wees, J.-D. (2020). Simulation of induced seismic ground motions using coupled geomechanical and seismic wave propagation models. *Geophysical Journal International*, *220*(2), 1284–1299.

Pampillón, P., Santillán, D., Mosquera, J. C., & Cueto-Felgueroso, L. (2018, jul). Dynamic and quasi-dynamic modeling of injection-induced earthquakes in poroelastic media. *Journal of Geophysical Research: Solid Earth*, *123*(7), 5730–5759. doi: 10.1029/2018JB015533

Ren, G., Jiang, J., & Younis, R. (2016a). Fully coupled geomechanics and reservoir simulation for naturally and hydraulically fractured reservoirs. In *50th us rock mechanics/geomechanics symposium.*

Ren, G., Jiang, J., & Younis, R. M. (2016b). A fully coupled xfem-edfm model for multiphase flow and geomechanics in fractured tight gas reservoirs. *Procedia Computer Science*, *80*, 1404–1415.

Ren, G., Jiang, J., & Younis, R. M. (2018). A Model for coupled geomechanics and multiphase flow in fractured porous media using embedded meshes. *Advances in Water Resources*, *122*, 113–130. doi: 10.1016/j.advwatres.2018.09.017

Ren, G., & Younis, R. M. (2018). A coupled XFEM-EDFM numerical model for hydraulic fracture propagation. *16th European Conference on the Mathematics of Oil Recovery, ECMOR 2018*.

Ren, G., & Younis, R. M. (2019). A numerical method for hydraulic fracture propagation using embedded meshes. *Society of Petroleum Engineers - SPE Reservoir Simulation Conference 2019, RSC 2019*.

Ren, G., & Younis, R. M. (2021a). An integrated numerical model for coupled poro-hydro-mechanics and fracture propagation using embedded meshes. *Computer Methods in Applied Mechanics and Engineering*, *376*, 113606. doi: 10.1016/j.cma.2020.113606

Ren, G., & Younis, R. M. (2021b). A quasi-newton method for physically-admissible simulation of poiseuille flow under fracture propagation. *arXiv preprint arXiv:2111.00264*.

Ren, G., & Younis, R. M. (2021c, 10). *A Time-Continuation Solver for Hydraulic Fracture Propagation.* (D011S007R001) doi: 10.2118/203937-MS

Rice, J. R. (1993). Spatio-temporal complexity of slip on a fault. *Journal of Geophysical Research: Solid Earth*, *98*(B6), 9885–9907.

Rice, J. R., & Ben-Zion, Y. (1996). Slip complexity in earthquake fault models. *Proceedings of the National Academy of Sciences*, *93*(9), 3811–3818.

Schwartzkopff, A. K., Sainoki, A., & Elsworth, D. (2021, nov). Numerical simulation of mixed aseismic/seismic fault-slip induced by fluid injection using coupled X-FEM analysis. *International Journal of Rock Mechanics and Mining Sciences*, *147*, 104871. doi: 10.1016/J.IJRMMS.2021.104871

Sheth, S., Heidari, M. R., Neylon, K., Bennett, J., & McKee, F. (2021). Acceleration of thermodynamic computations in fluid flow applications. *Computational Geosciences*, 1–11.

Sheth, S. M., & Younis, R. M. (2017). Localized linear systems in sequential implicit

830   simulation of two-phase flow and transport. *SPE Journal*, *22*(05), 1542–1569.

831   Ţene, M., Bosma, S. B., Al Kobaisi, M. S., & Hajibeygi, H. (2017). Projection-based
832   embedded discrete fracture model (pedfm). *Advances in Water Resources*, *105*,
833   205–216.

834   Thomas, M. Y., Lapusta, N., Noda, H., & Avouac, J.-P. (2014, mar). Quasi-dynamic
835   versus fully dynamic simulations of earthquakes and aseismic slip with and
836   without enhanced coseismic weakening. *Journal of Geophysical Research: Solid
837   Earth*, *119*(3), 1986–2004. doi: 10.1002/2013JB010615

838   Torii, A. J., & Machado, R. D. (2012). Structural dynamic analysis for time re-
839   sponse of bars and trusses using the generalized finite element method. *Latin
840   American Journal of Solids and Structures*, *9*(3), 1–31.

841   Wynants-Morel, N., Cappa, F., De Barros, L., & Ampuero, J.-P. (2020). Stress
842   perturbation from aseismic slip drives the seismic front during fluid injection in
843   a permeable fault. *Journal of Geophysical Research: Solid Earth*, *125*(7).

844   Xu, S., Ren, G., Younis, R. M., & Feng, Q. (2021). Revisiting field estimates for car-
845   bon dioxide storage in depleted shale gas reservoirs: The role of geomechanics.
846   *International Journal of Greenhouse Gas Control*, *105*, 103222.

847   Younis, R., & Aziz, K. (2007). Parallel automatically differentiable data-types for
848   next-generation simulator development. In *Spe reservoir simulation sympo-
849   sium.* doi: 10.2118/106493-MS

850   Younis, R., Tchelepi, H. A., & Aziz, K. (2010). Adaptively localized continuation-
851   newton method—nonlinear solvers that converge all the time. *SPE Journal*,
852   *15*(02), 526–544.

853   Younis, R. M. (2011). *Modern advances in software and solution algorithms for
854   reservoir simulation.* Stanford University.

855   Younis, R. M., & Tchelepi, H. A. (2012). Lazy k-way linear combination kernels
856   for efficient runtime sparse jacobian matrix evaluations in c++. In *Recent ad-
857   vances in algorithmic differentiation* (Vol. 87, pp. 333–342). Springer. doi: 10
858   .1007/978-3-642-30023-3_30